EXPERIMENTAL AND NUMERICAL INVESTIGATIONS ON COMPACT PLATE HEAT EXCHANGER

A Thesis

by

Erdem Peçenek

Submitted to the
Graduate School of Sciences and Engineering
In Partial Fulfillment of the Requirements for
the Degree of

Master of Science

in the
Department of Mechanical Engineering

Özyeğin University
August 2019

EXPERIMENTAL AND NUMERICAL INVESTIGATIONS ON COMPACT PLATE HEAT EXCHANGER

Approved by:

_____

Dr. Özgür Ertunç, Advisor
Department of Mechanical Engineering
Özyeğin University

_____

Dr. Altuğ Melik Başol
Department of Mechanical Engineering
Özyeğin University

_____

Prof Dr. Hojin Ahn
Department of Mechanical Engineering
Yeditepe University

Date Approved: 15 August 2019

To my family and friends

ABSTRACT

The objective of this thesis was to understand flow phenomena inside chevron type plate heat exchangers. To reach this goal, several visualization experiments designed and conducted. Also Large eddy flow simulations were made. This simulations validated with visualization experiments and pressure drop experiments. The flow visualization results showed that rather than helical or cross flow structure, a combination of two structures exists inside the CPHE channel geometry. Visualization and pressure drop experiments validated the LES results. LES estimated the friction factor with maximum 5 percent error. Mixing study proved there is asymmetric mixing through the channel. To understand transition inside the channel a power spectrum of velocity magnitude of specified points was reported and results showed that between $Re = 265$ and $Re = 275$ there is a significant raise at turbulent intensity where seems the transition takes place.

ÖZETÇE

Bu tezin amacı, chevron tipi plakalı ısı eşanjörleri içindeki akış olaylarını anlamaktır. Bu hedefe ulaşmak iin çeşitli görselleştirme deneyleri tasarlandı ve uygulandı. Ayrıca türbülans modeli olarak Large eddy simülasyonu kullanan sayısal simülasyonlar yapılmıştır. Bu simülasyonlar görselleştirme deneyleri ve basınç düşüm deneyleriyle doğrulanmıştır. Akış görselleştirme sonuçları, sarmal veya çapraz akış yapısı yerine, CPHE kanalı içinde iki yapının bir kombinasyonunun bulunduğunu göstermitir. Görsel deneyler LES sonuçları dorulandı. LES, sürtünme faktörünü maksimum yuzde 5 hatayla tahmin etti. Karışım üzerine yapılan çalışma, kanal boyunca asimetrik bir karışım olduğunu kanıtladı. Kanal içerisindeki akışın bir rejimden diğerine geçişini anlamak amacıyla daha önce belirlenen noktalardaki mutlak hızların gç spectrum grafiği belirtilmiştir. Bunun dışında sonuçlar turbulent intensity'nin $Re = 265$ ve $Re = 275$ arasnda dikkate değer bir sıçrama yaptını gösteriyor ve sıçramanın olduğu bu aralıkta rejimler arası geçiş gerçekleşmiş gibi gözüküyor.

ACKNOWLEDGEMENTS

TABLE OF CONTENTS

LIST OF TABLES

LIST OF FIGURES

Nomenclature

Greek and Roman Symbols

α -Solution variable

β -Chevron angle (°)

$\triangle$ -Filter width (m) $(\Delta_x \Delta_y \Delta_z{}^{1/3})$

ΔP -Pressure drop (Pa)

γ -Aspect ratio (-)$(\frac{4 \times a}{\lambda}$ or $\frac{a}{\lambda})$

κ -von Karman constant

λ -Corrugation pitch (m)

μ -Dynamic viscosity (Pa.s)

ϕ or φ -Surface enlargement factor (-)

ϕ_i -Passive scalar component

ρ -Density (kg/m^3)

σ -Schmidt number

σ_t -Turbulent Schmidt number

α' -Subgrid value of solution variable

μ_t -Subgrid scale turbulent viscosity (Pa.s)

$\tilde{\alpha}$ -Filtered value of solution variable

Other Symbols

$\dot{m}$ -Mass flow rate (kg/s)

       -Average velocity

$\mathbf{I}$ -Identity tensor

$\mathbf{j}_i$ -Diffusion flux

$\mathbf{S}$ -Mean stress tensor $(\frac{1}{2}(\triangledown\bar{\mathbf{v}} - \triangledown\bar{\mathbf{v}}^T))$

$\mathbf{T}$ -Stress Tensor

$\mathbf{T}_t$ -Turbulent stress tensor

$\mathbf{v}$ velocity (m/s)

$\mathbf{v}_{fluc}$ -Velocity fluctuation (m/s)

a -Corrugation amplitude (m)

C_w -Model coefficient

k -Subgrid scale turbulent energy

Re -Reynolds number (-) $(\frac{G_c \times D_h}{\mu})$

S_w -Deformation parameter

S_{ϕ_i} -Passive scalar source term

t -Plate thickness (m)

V -Cell volume m^3

$\tilde{\mathbf{v}}$ -Filtered velocity (m/s)

A_C -Cross section of channel (m)

D_h -Hydraulic diameter (m) $(\frac{2 \times a}{\varphi})$

D_p -Port diameter (m)

f -Friction factor (-) $(f = 2\Delta P A_c^2 \frac{D_h}{L_v} \frac{\rho}{\dot{m}^2})$

G_c -Mass velocity (kg/m^2.s) $(\frac{\dot{m}}{a \times L_w})$

L_v -Distance between ports (m)

L_w -Channel width (m)

CHAPTER I

INTRODUCTION

Plate heat exchanger is a heat exchanger type. The first plate heat exchangers appeared in 1880s, when there was a need for new type of heat transfer equipment that can handle the harsh requirements of pasteurization process. In those years, people were affected by deadly diseases such as tuberculosis frequently. One of the reasons caused tuberculosis was raw milk consumption. Pasteurization process, heats the milk up to high temperatures and cool down immediately. This process kills bacteria inside milk, without changing the taste of milk. However, to be able to treat milk, an efficient heat exchanger in need. First plate heat exchangers occurred in such environment. In time plate heat exchanger designs and manufacturing methods developed. First it was used in food industry, then with these improvements it became considerable in other industries such as, refrigeration, air conditioning, refinery and petrochemical systems etc. [Wang et al., 2007].

Plate heat exchangers have many advantages over traditional heat exchangers. High heat transfer coefficients is one of them. The flow inside plate heat exchanger channels has low critical Reynolds number. The complex flow inside channels provides turbulence even at low Reynlods numbers (Re=500), which provides high heat transfer coefficients. Also the plate corrugations and patterns provide high heat transfer areas. These properties enable to have same heat transfer load in a lower amount of space when it is compared to other heat exchangers. Another advantage of this type of plate heat exchangers is low fouling rates [Wang et al., 2007].

One of the objectives of this study is analyzing the flow inside a chevron type plate heat exchanger. To analyze the flow, visualization experiments and Large eddy

simulations conducted. Another objective is to understand the transition phenomena inside the channel. In this work, an upscaled channel used, to be able to conduct visualization experiments. The knowledge that provided by this work will generate a know-how in local industry. The plate heat exchangers used in many different applications, such as, refrigeration, heat pumps, boilers, food industry etc. Knowledge gained from this study might be used in these applications. The next generation of these devices might be designed inside the country with the help of the experiences gained from this research.

1.1 History

As mentioned before, first plate heat exchangers designed in 1880s. The trigger was the need for high efficient heat exchangers, that can be used for pasteurization processes. First patent was taken by Albrecht Drake in 1878 [Wang et al., 2007]. In following years, plate heat exchanger designs continued to develop and in 1920s first operational plate heat exchanger invented by Dr. Richard Seligman , the founder of APV International. With recent developments in manufacturing methods, they became available for various different industrial applications.

1.2 Literature Survey

1.2.1 Basics

In CPHEs, simply the hot and cold fluid flows inside adjacent channels where heat exchange happens between mediums. The channel between two plates (with opposite directions) provides high heat transfer coefficients and the transition from laminar to turbulence occurs in low Reynolds numbers ($\cong 500$ Re) with correspond to other heat exchanger types. Also the corrugated plates provides a significant amount of heat transfer area. Another feature of plate heat exchangers is they can easily be dismounted, which provides ease of cleaning. This feature is especially important for the hygienic applications. However, the operating conditions, such as, maximum

pressure and maximum temperature provide limits for the applications where plate heat exchangers used. In time with developments in manufacturing techniques these limits overcomed. Some present versions of plate heat exchangers are mentioned below [Wang et al., 2007].

- Gasketed plate heat exchanger: In gasketed plate heat exchangers, channels between plates sealed with gaskets and the frame includes bolts and bars to stack plates.

- Brazed plate heat exchanger: In this type, a brazed material such as copper used. In the end of the brazing process metal plates brazed to each other at several points. The difference between gasketed plate heat exchanger is, there are no frames or gaskets in brazed plate heat exchangers. There are several different brazing materials can be used for process (Nickel etc.). The advantage of this type they can work at high temperature (max. 400 C) and high pressure (max. 30 bar) conditions and with the absence of frame, the weight of heat exchanger is much lower.

- Semi-welded plate heat exchanger: The plates are welded in pairs in this type. The weldings increased the maximum pressure and temperature that system can handle. This type especially good for corrosive mediums, since the gaskets contact with fluid only at the ports.

- Fully-welded plate heat exchanger: Different than semi-welded plate heat exchangers, this time plates are completely welded. Gaskets are in no use. Again the maximum temperature and pressure conditions that can be handled are improved. However the design lost its flexibilty, since the plates cannot be increased nor decreased.

- Wide-gap plate heat exchanger: Gaps between the plates are higher in this

version. This feature is desirable for high viscosity fluid applications.

- Diabon-graphite plate heat exchanger: Plates are made of graphite in this type of heat exchanger. This property is useful, especially for corrosive fluids that metal and alloys cannot handle.

- Minex plate heat exchanger: Miniature version of gasketed plate heat exchanger.

	Gasketed	Brazed	Semi-welded	Fully welded	Wide gap	Double wall	Diabon graphite
Operating conditions							
Pressure [bar]	2.5	3.0	2.5	4.0	0.9	2.5	0.6
Temperature [°C]	30–200	−195–225	−30–200	−200–350	30–200	30–200	0–140
Type of service applicability							
Liquid–liquid	E	E	E	E	E	E	E
Gas–liquid	G–P[a]	E	E–P	E–P	G–P	G–P	E–P
Gas–gas	M–P	G–P	G–P	G–P	M–P	M–P	E–M
Condensation	G–P	E	E–M	E–M	E–M	E–M	E–M
Evaporation	G–P	E	E–M	E–M	E–M	E–M	E–M
Nature or type of fluid media							
Corrosive/aggressive	M–P	M–P	E	E	M	M	E
Viscous	E	M–P	E	G–M	E	E	M
Heat sensitive	E	E	E	E	E	E	E
Hostile reaction	M–P	M	G	G	M–P	E	G–M
Fibrous	P	P	P	P	E	P	P
Slurries	M–P	P	M	M	G	M	M
Fouling	G–M	M	M	M	G	M	M
Maintenance flexibility							
Mechanical cleaning	B	N	O	N	B	B	B
Repair	B	N	O	N	B	B	B
Modifications	B	N	O	N	B	B	B

Notes: E – excellent, G – good, M – moderate, P – poor, B – both sides of plate, O – one side of plate, N – no side of plate.
[a]Depending upon the operating pressure and gas/vapour density.

Figure 1: A selection guide of PHEs for different operating and service conditions [Wang et al., 2007]

This different types of plate heat exchangers offers different features that are

useful depending on the application. The most important parameter is maximum temperatures and maximum pressures that plate heat exchanger can handle. Some of the properties are listed in the table provided by [Wang et al., 2007] , represented below in Figure 1.

1.2.1.1 Plate Geometry

The plate geometry defines the performance of the plate heat exchangers. Plate geometry of a CPHE is a complex one. In this section, the parameters will be represented in two groups which are corrugation parameters and plate parameters.
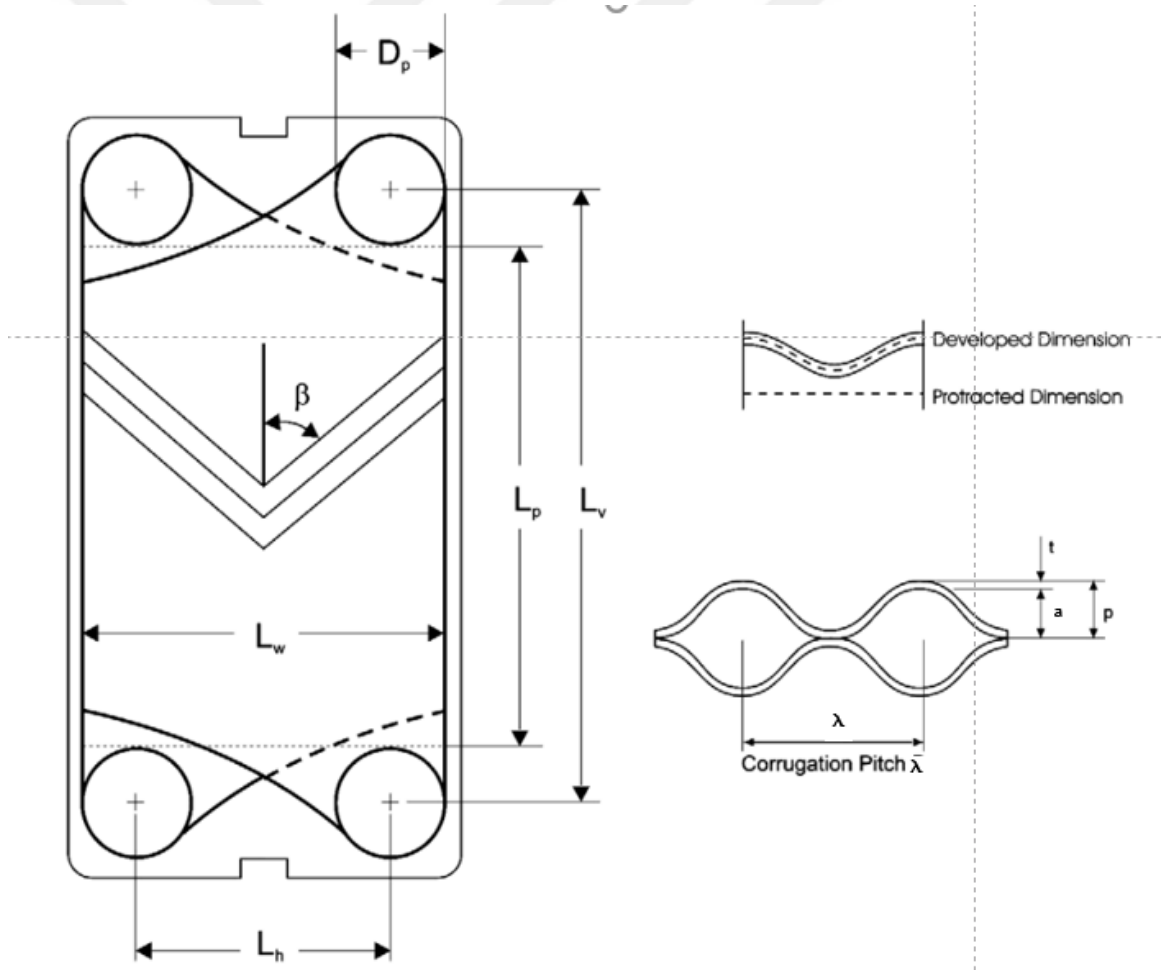
Figure 2: Chevron type plate geometry [Khan et al., 2010]

Corrugation parameters:

Chevron angle (β): The angle between the flow direction and corrugation direction.

Corrugation pitch (λ): Distance between two peaks of periodic corrugation shapes.

Corrugation amplitude(a): Amplitude of the sinusoidal wave.

Aspect ratio(γ): Definition of aspect ratio, differs from author to author. Metwally and Manglik [Metwally and Manglik, 2004] defined it as ($4a/\lambda$), for Dovic et al. [Dović et al., 2009] the definition is (a/λ)

Plate thickness(t): Thickness value of the plate

Surface enlargement factor(φ): Ratio of developed surface area to projected area. It is a function of amplitude and corrugation pitch.

$$\varphi = \frac{1}{6}[1 + \sqrt{((1 + (\frac{\pi\gamma}{2})^2)}] \tag{1}$$

Corrugation cross section: Corrugation cross section is one of the important parameters that affect hydrodynamic and thermal characteristics of the channel. Some of the used cross sections are triangular, sinusoidal, trapezoidal, elliptic, rectangular etc.
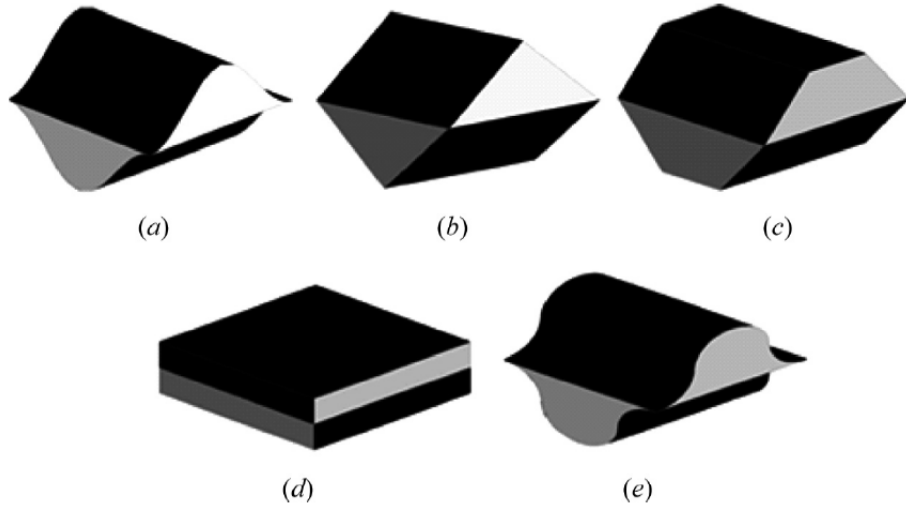
Figure 3: Chevron corrugated plate pattern [Zhang and Che, 2011]

Plate parameters:

Plate width (L_w): Width of the channel

Plate length (L_v): Vertical distance between ports.

Port diameter (D_p): Diameter of ports

Plate number: Number of plates used in heat exchanger

Corrugation pattern: There are different types of corrugation patterns as chevron, washboard, oblique washboard, herringbone etc. as presented in Figure 4.

(a) (b) (c) (d) (e) (f)
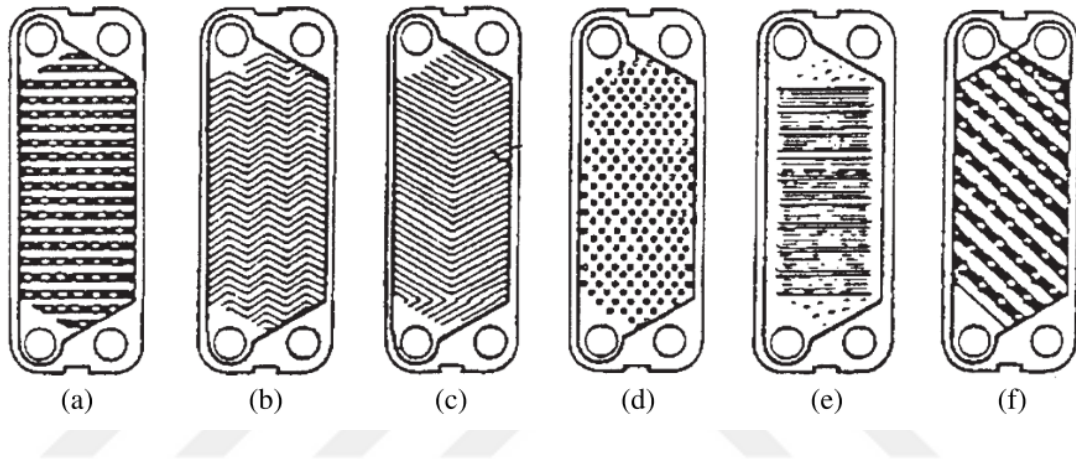
Figure 4: Chevron corrugated plate pattern [Wang et al., 2007]

1.2.1.2 System

Plate heat exchanger system has various configurations. There are different parameters such as flow direction, flow distribution, passes, plate types etc.

Flow directions can be parallel or counter flow as in Figure 5. The flow is towards to same direction at both sides of the plate in parallel flow, while it has opposite directions at different sides of the plate in counter flow. Pass types can be single pass or multipass. Difference of multipass and single pass can be seen in Figure 6. Also there are different flow distribution options. These are U and Z type flow distributions, as in Figure 6. Plate options are increased with the developments in plate design, Plate types can be categorized as in Figure 1. In this figure the suitability of the plate types is given.
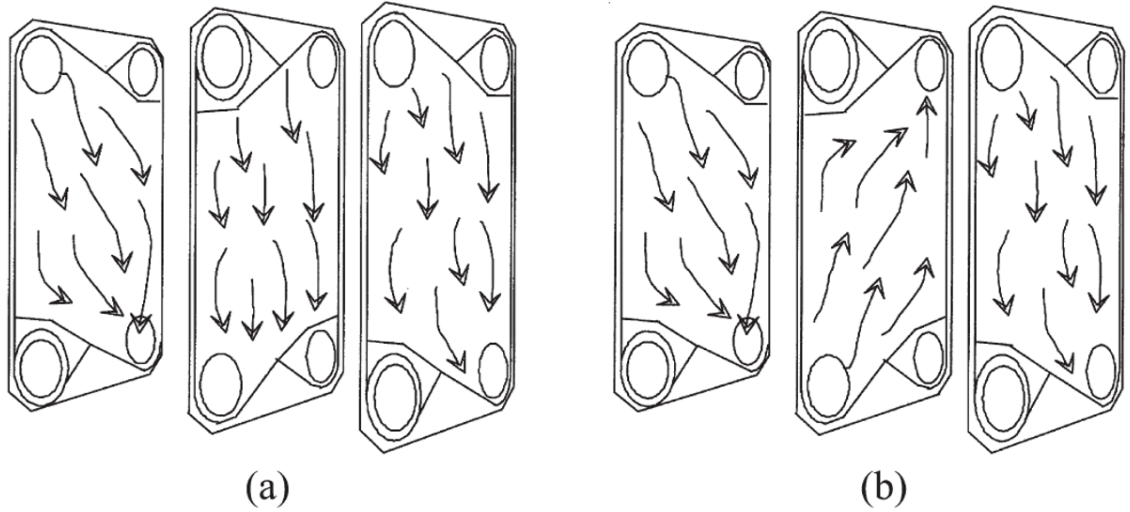
Figure 5: Flow arrangements (a) Parallel and (b) Counter-flow [Wang et al., 2007]

(a)

(b)

(c)
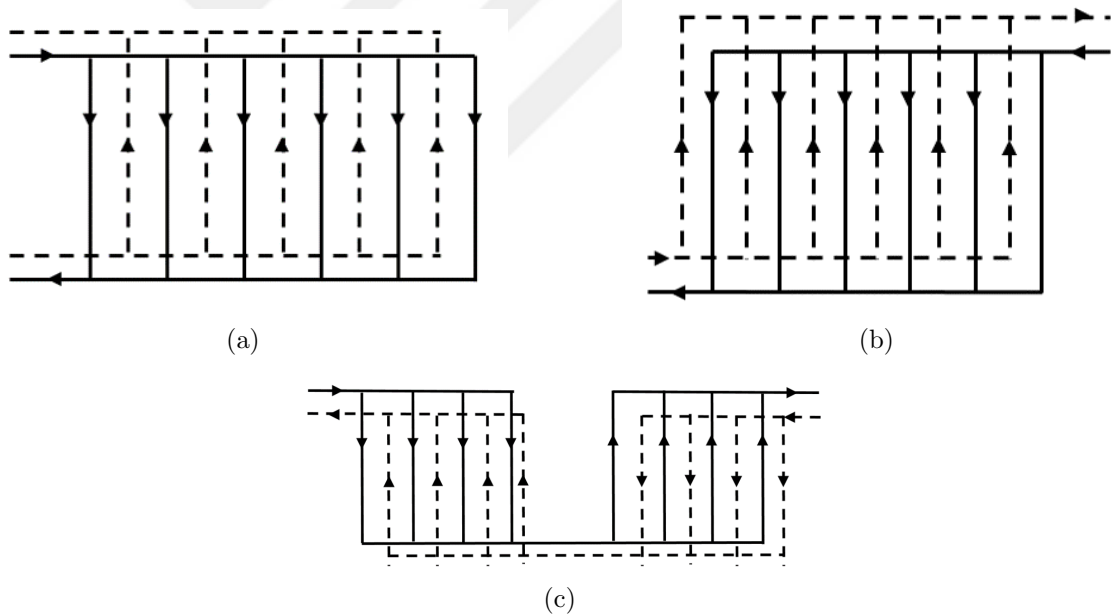
Figure 6: U and Z arrangement of channels (a) U type single pass, (b) Z type single pass, (c) Multipass (2 pass/ 2 pass flow system)

1.2.1.3   Working principles

In plate heat exchangers, there are hot and cold fluid, and these fluids pass from the adjacent channels. Adjacent plates are rotated by 180 degrees. The flow represented

in Figure 7.
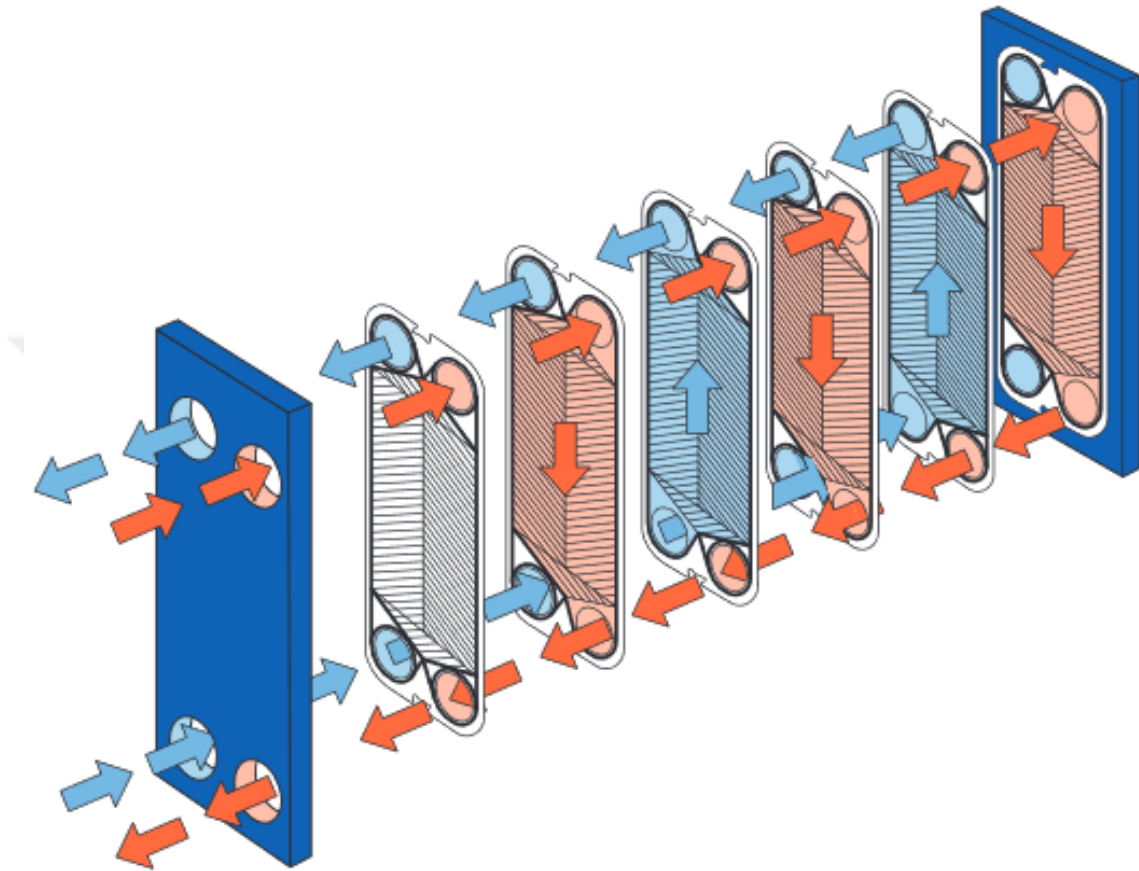
Figure 7: Flow inside a CPHE

1.2.1.4   Advantages

Main advantages of a plate heat exchanger are high heat transfer areas and high heat transfer coefficients. The presence of the corrugations increased the heat transfer area significantly when it is compared to a flat plate. Another advantage is high heat transfer coefficients. Plate heat exchanger channel has a unique geometry, that forces the flow to be turbulent at low Reynolds number.

1.2.2 Correlations

There are many experimental correlations exist in literature and the reason is the complex channel geometry of plate heat exchangers. Change in one of the geometry parameter, makes the correlation less accurate. Because of this issue, generally authors use their own correlations. Different correlations for various channel geometries exist in literature. The review of Ayub represented 41 correlations [Ayub, 2003] . Very few of the studies concentrate to create a general correlation or a model to predict the pressure drop and heat transfer in plate heat exchanger channels. Martin [Martin, 1996] and Dovic et al. [Dović et al., 2009] came up with semi-empirical model and generalized correlation respectively.

Martin [Martin, 1996] came up with semi-empirical equations for Nusselts number and friction factor. The study used flow visualitions of Focke and Knibbe [Focke and Knibbe, 1986] and Gaiser and Kottke [Gaiser and Kottke, 1990] while creating the equation. The equation 2

$$Nu = \phi \cdot 0.122 \cdot Pr^{1/3} \cdot (\frac{\mu}{\mu_w})^{1/6} \cdot [\xi \cdot (\frac{Re}{\phi})^2 \cdot \sin(2 \cdot \varphi)]^{0.374} \tag{2}$$

$$\frac{1}{\xi} = \frac{\cos \varphi}{\sqrt{0.18 \tan \varphi + 0.36 \sin \varphi + \xi / \cos \varphi}} + \frac{1 - \cos \varphi}{\sqrt{3.8 \cdot \xi_{1,0}}} \tag{3}$$

Dovic et al. [Dović et al., 2009] created a mathematical model and adjusted this model to experimental heat transfer and pressure drop results of other authors. In their study first modeled the characteristic length of flow components which are cross and longitudinal flow. Then they modeled the Nusselts number and friction factor.

There many different correlations present in literature, so only few of them will be presented here. There are some review papers that presented most of the correlations in literature like Ayub's [Ayub, 2003].

Author	Re range	Fluid	Chevron angle	Friction factor
Savostin and Tikhonov	$200 \leq Re/\phi \leq 600$	air	$0° \leq \beta \leq 33°$	$f = 6.25(1 + 0.95\psi^{1.72})\phi^{1.84}Re^{-0.84}$
	$600 \leq Re/\phi \leq 4000$			$f = 0.925[0.62 + 0.38\cos(2.6\psi)]\phi^{1+a_2}Re^{-a_2}$ $a_2 = 0.53[0.58 + 0.42\cos(1.87\psi)]$
Tovazhnyanski et al.	$2000 < Re < 25000$	-	$\beta = 30°, 45°, 60°$	$f = 0.085 \exp[1.52tan\beta]\, Re^{-(0.205-0.06tan\beta)}$
Chisholm and Wannirachi	$1000 < Re < 4000$		$30° \leq \beta \leq 80°$	$f = 0.08Re^{-0.25}\phi^{1.25}(\beta/30)^{3.6}$
Heavner et al.	$400 < Re\phi < 10000$		$\beta = 45°/90°$	$f = 1.75\phi^{1.0838}Re^{-0.0838}$
			$\beta = 23°/90°$	$f = 1.64\phi^{1.1353}Re^{-0.1353}$
			$\beta = 45°/45°$	$f = 0.810\phi^{1.1405}Re^{-0.1405}$
			$\beta = 23°/45°$	$f = 0.649\phi^{1.1555}Re^{-0.1555}$
			$\beta = 23°/23°$	$f = 0.571\phi^{1.1814}Re^{-0.1814}$
Talik et al.	$10 < Re < 80$	-	$\beta = 60°$	$f = 12.065Re^{-0.74}$
	$1450 < Re < 11460$		$\beta = 60°$	$f = 0.3323Re^{-0.042}$
Muley and Manglik				

Table 1: Friction factor correlations [Ayub, 2003]

Author	Re range	Fluid	Chevron angle	Friction factor
Muley and Manglik	$Re < 16$	-	$\beta = 60°$	$f = 51.5/Re$
	$16 \leq Re \leq 100$			$f = 17.0\, Re^{-0.6}$
	$Re \geq 800$			$f = 2.48\, Re^{-0.2}$
Muley and Manglik	$2 \leq Re \leq 200$	-	$\beta = 30°/60°$	$f = [(40.32/Re)^5 + (8.12\, Re^{-0.5})^5]^{0.2}$
	$Re \geq 1000$			$f = 1.274\, Re^{-0.15}$
Muley and Manglik	$Re \geq 1000$	-	$30° \leq \beta \leq 60°$	$f = [2.917 - 0.1277(90 - \beta) + 2.016 \times 10^{-3}(90 - \beta)^2] \times [5.474 - 19.02\phi + 18.93\phi^2 - 5.341\phi^3] \times Re^{-[0.2+0.0577\sin\left(\frac{\pi(90-\beta)}{45}\right)+2.1]}$
Kumar	$Re < 10$	water	$\beta \leq 30°$	$f = 50.0/(Re)^{1.0}$
	$10 < Re < 100$			$f = 19.40/(Re)^{0.589}$
	$Re > 100$			$f = 0.810\phi^{1.1405}$
	$Re < 15$		$\beta = 45°$	$f = 47.0/Re^{1.0}$
	$15 < Re < 300$			$f = 18.29/Re^{0.652}$
	$Re > 300$	-		$f = 1.441/Re^{0.206}$

Table 2: Friction factor correlations [Ayub, 2003]

1.2.3 Flow visualizations

Flow visualization studies played a significant role to understand the flow mechanisms inside CPHE channels. There are few flow visualization studies in literature, most popular ones are Focke and Knibbe (1986) , Dovic et al. (2009)and Kottke and Gaiser (1990) . These flow visualization studies defined the flow characteristics in a CPHE channel. Authors demonstrated flow structures in their flow visualization studies. Analysis of these flow structures, at different channel geometries, are present in literature.
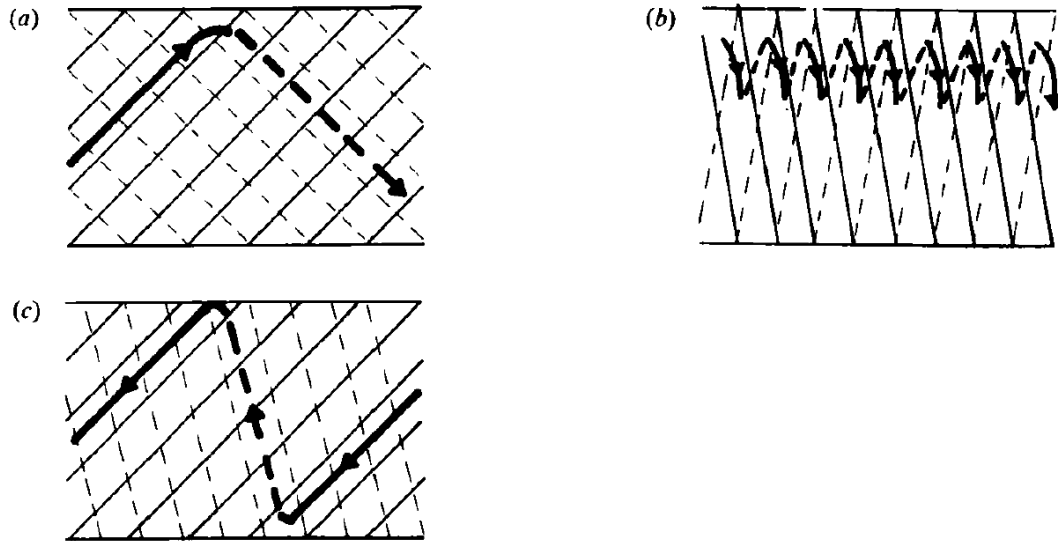
Figure 8: Flow inside a CPHE a cphe channel (a) 45°/45°, (b) 80°/80° , (c) 45°/80°

Dovic et al. (2009) used two different plates in his study, β =28° and β=61° . The study categorized the flow structures in two which are longitudinal wavy and furrow flow. The visualization experiments have done between 0.1-250 Re. Effect of injection location, Reynolds number, chevron angle, viscosity were mentioned in study. Dovic and Svaic (2007) presented that when Reynolds number increases, the furrow component increases. Furthermore, this work compared injection locations for β=28° . Injection close to wall and middle of the cross section was compared. The

results showed that at centre flow structures were more likely to have longitudinal flow structure. In Dovic et al. (2009) different fluids were used (aqueous glycerol and water). It is mentioned that $\beta \leqslant 45$ furrow flow pattern prevails, $\beta \geq 60°$ will be predominantly wavy longitudinal.

Dovic et al. (2007) mentions that at higher Reynolds numbers, higher aspect ratio (b/l), lower chevron angle will promote furrow flow. Stronger mixing can be expected higher β, higher Re, lower aspect ratio.

1.2.4 Effect of parameters on heat transfer and pressure drop

Focke et al. (1985) used 0° , 30° , 45° , 60° , 72° , 80° and 90° chevron plates in their study. They created friction factor and Colburn j factor correlations for these channels. The article reported that with increasing chevron angle (at constant Re) leads to pressure drop increases over two and a half order of magnitude while heat transfer increases factor of $4 - 10$. For the plates $30° \leqslant \beta \leqslant 60°$ cross flow structure exists. For 80° the pressure drop and heat transfer are their maximum. But in 72° marginally higher.

Muley and Manglik (1999) worked with 30° /30° , 30° /60° , 60° /60° . Study represented that there is up to five times and 44 times enhancement when it is compared to an equivalent flat plate. Correlation was influenced by Re, Pr, μ /μ, β, ϕ and it is valid for Re ≥ 1000, $30° \leqslant \beta \leqslant 60°$ and $1 \leqslant \phi \leqslant 1.5$.

T.S Khan et al. (2010) again used 30° /30° , 30° /60° , 60° /60° . In this work, it is mentioned that at a given Re, Nu increases four to nine times compared to flat plate. Study mentions that enhanced heat transfer of a corrugated plate heat exchanger is due to higher turbulence levels rather than the surface enlargement.

Dovic and Svaic (2007) reported the effect of aspect ratio to friction factor and Nusselts number with increasing chevron angle. The results show that at lower chevron angle than 40° effect of aspect ratio is very low. For 60° chevron angle,

the effect of aspect ratio is greater. With increasing Reynolds number the influence of the aspect ratio becomes greater.

Kanaris et al. (2009) reported that at Re=6000 channel as the channel aspect ratio increases while friction losses increases linearly, the heat transfer augmentation with respect to a smooth surface.

Metwally and Manglik (2004) made numerical study in 10-1000 Re range. They mentioned that with increasing aspect ratio greater friction factor was attained. Also with increase in Reynolds number, the friction factor decreases and converges at some point. For Nusselts number, with increasing aspect ratio the Nusselts number increases and the higher the Reynolds number, the higher the Nusselts number.

Zhang and Che (2011) had studied the effect of corrugation profiles. In their work, velocity fields, temperature fields, local Nusselts number distribution, friction factor and Nusselts number for different corrugation profiles (trapezoidal,rectangular, triangular, sinusoidal, elliptic) was reported. They used low Reynolds number k-ϵ model and representative unitary cells as domain. The results showed that maximum f of trapezoidal profile is about four times greater than the smooth corrugation profiles (sinusoidal, elliptic). For sharp corrugation profiles (trapezoidal, rectangular, triangular), there is a considerable difference of f values between rectangular and triangular profiles. Lowest f values occurred in smooth profiles. There is significant change variation of f values between sharp and smooth corrugation profiles.

Most of the articles in literature focus on symmetric plate configurations. Only few articles such as Muley and Manglik (1999) used asymmetric plates. Ciofalo et al. (1996) studied the effect of undulation(lower plate) geometry in asymmetric configurations. In their work, the corrugated plate (upper plate) kept the same and parallel to the main flow direction and the pitch, height and chevron angle of the undulation changed. The effect of pitch and height value analyzed for different chevron angles. Simply, they have used same pitch value and different undulation heights for multiple

chevron angles. The experimental results have shown the corrugated plate Nu is lower than undulated plate Nu, except one plate (UCS) which has deep undulations. It is mentioned that Nusselts number for corrugated and undulated plate increased with undulation chevron angle, but this dependency is lower when it is compared with symmetric configurations. Nu becomes higher when undulation height increases, however, does not change much with the undulation pitch. So far the effects on heat transfer is discussed, but undulations have also significant effect on friction factor and pressure drop. Friction factor coefficients are scattered more than heat transfer results. It is hard to put full range of Re into a power-law. Article mentioned that Re dependence followed -0.5 power-law generally for Re < 3000 and weaker at higher Re's. Influence of chevron angle on friction factor is more significant than on Nu. From 20° to 70° f increased increased 2 to 3 times. However, the effect of chevron angle on symmetric configurations still greater than corrugated-undulated configurations.

Transition inside the CPHE channels are open discussion in literature. Because of the complex geometry of channels, changes in geometrical parameters affects the transition. Several authors made comments on the topic. Focke et al. (1985) mentions that when chevron angle is zero, the main flow becomes turbulent around Re = 200. For 80° chevron angle, he says the flow becomes more complex and this leads to a transition at lower Reynolds Numbers. For 90 degree chevron angle, this time it is mentioned that flow becomes turbulent below Re = 300. Blomerius et al. (1999) studied the transition in their article. It is shown that, with increasing Reynolds numbers from steady to periodic oscillatory flows transition takes place. Exact Reynolds number for transition is not known, but authors believe it lies between 170 Re and 255 Re for λ/a^*=7 and λ/a^*=7. Fourier analysis of the study has shown that at Re=255, there is a periodic flow. Around Re=425 dominant St=1.3. Lastly for Re=1700 St=0.5 the flow is turbulent. As a result of their parametric study, the results have

shown that at larger wavelengths the transition takes place at higher Reynolds numbers. Wang et al. (2007) mentions the critical Reynolds numbers based on the sharp changes at friction factor. While sharp change occurs at Re=948 for 60° chevron angle, it occurs at Re=1284 for 120 degrees chevron angle. Focke (1983) mentions that there is an early transition to turbulence present inside CPHE channels takes places between Re = 10 to Re = 500. Croce and D'Agaro (2002) studied transition numerically, using a representative cell. They observed that Re < 300 the flow is steady and and Re>350 it is unsteady. They make comment on the transition based on f and Nu values. It is said that transition from steady to unsteady occurred where sharp change occurred on f and Nu which corresponds to somewhere around Re = 300.

There are several numerical studies present in literature, which have used various plate geometries and turbulence models. Han et al. (2011) showed most of the popular numerical studies in their literature survey and said generally a unitary cell was used in the studies because of the high computational costs. In their study they used a corrugation channel instead of an entire plate and by using Shear stress transport(SST) model they come up with maximum $\mp$ 20 percent deviation. Ciofalo et al. (1996) used many different models on a unitary cell such as LES, laminar, low Reynolds k-epsilon, k-epsilon. The study shows effects of Reynolds number, chevron angle and aspect ratio on flow in range of 100 to 1000 Reynolds number. Results proved that k-epsilon model with wall functions might be used for high flow rates or high chevron angles. The model cannot predict entry effects and it is mentioned that it should not be applied to lower Reynolds numbers lower than 2000. The research also focuses on flow fields, it is mentioned that relative intensity of swirling flows increases with Re, chevron angle and pitch to height ratio. The complexity of swirling flow increases with Re, chevron angle and decreases with pitch to height ratio. The research mentioned that at the moderate Re and chevron angle used

geometry has better heat transfer performance without causing significant pressure drop penalty.Metwally and Manglik (2004) has used 90 degree chevron angle plates and analyze the effect of aspect ratio and Reynolds number to flow structures and heat transfer. It seems both amplitude, pitch and Reynolds number had significant effect on flow structures. It is reported that with increasing amplitude or decreasing pitch fluid recirculation and swirl flows increases and these lateral vortex grows with aspect ratio. Sarraf et al. (2015) used a entire brazed plate heat exchanger channel and unitary cell in their study. Flow was investigated inside the channel. The results showed that at 55 degrees chevron angle channel when Re = 21 the helical flow structure dominates the flow and when Re = 2100 the cross flow structure is dominant. Another focus of the study is defining which flow structure dominates at which Reynolds number. A unitary cell used for this and the results showed from Re = 0 to Re = 10 the helical structures are dominant, between 10 and 100 there is no dominance of a single structure and from 100 to around 2000 the cross flow structure is dominant.

1.2.5 Heat transfer enhancement methods

In this section, optimal configuration and plate dimension parameter selection will not considered as enhancement methods. Results of the studies that used different plate geometries such as different embossing types and modification of secondary corrugations. The review of Zhang et al. (2011) reported some studies that used different plate geometries than the most common chevron or herringbone plates. Such as, capsule-type, dimple-type, chevron-type, elliptic-type, round-type embossings ; double wave plates; and secondary corrugations (in-phase, anti-phase and full-wave rectified).

Zhang et al. (2016) made numerical study which used capsule type embossing. In their study, they used incompressible water as working fluid, the computational

domain is a unit cell with periodic boundary conditions. As turbulence model authors used SST- k ω model. The simulation conducted between 500-12470 Reynolds numbers. Results have shown that at Re$\leqslant$ 3000, capsule-type plate has the greatest Nu and second greatest at Re$\geq$3000. Pressure drop is the lowest in whole range.

Jeong et al. (2009) used three different type of plates. Such as, chevron embossed, elliptic embossed and round embossed. Working fluid was H2O/LiBr solution in numerical study. Solution has LiBr composition 54-62 percent in mass. Semi- Implicit Method for Pressure Linked Equations(SIMPLE) used for turbulent flow calculations. From the results, it seems that δP of elliptic and round embossing are lower. For heat transfer, the results have shown that round embossing has the worst heat transfer rate, elliptic embossing has the highest heat transfer rate and chevron type embossing are in between somewhere very close to elliptic ones in terms of heat transfer. For pressure drop, chevron embossing has the greatest value. This time elliptic and round embossing have great advantage over chevron embossing.

Durmus et al. (2009) three different plates, which are flat plate heat exchanger, corrugated plate heat exchanger and asterisk plate heat exchangers. Simply their often effects on heat transfer and friction factor. The work mentioned that the experiments were conducted in $50 \leqslant \text{Re} \leqslant 1000$ range. The range of Re considered as laminar flow conditions. $3 \leqslant \text{Pr} \leqslant 7$ represented the ranges of Prandtl number in experiments. $\text{Nu}/\text{Pr}^{1/3}$ versus Re graph, determines that corrugated PHE has the highest heat transfer rate at same Re. Asteriks PHE stands between corrugated PHE and plate PHE. F versus Re graph showed that Asterisk PHE had lower δ P than the corrugated PHE. When chevron corrugation PHE compared to asterisk PHE, it seems, it has 17 percent higher Nu and 40 percent higher δ P. When asterisk PHE and chevron PHE was compared to flat one, the increase was reported in δ P.

Kim et al. (2010) used double-wave plate in their study. Water and air used as working fluids through the study. The results of the experiments in this research

showed that double-wave PHE's have 50 percent higher heat transfer performance at air-side, however also its pressure drop 30 percent more than single-wave PHEs.

Doo et al. (2012) made a research where they used three different types of secondary corrugations, which are in-phase, anti-phase and full-wave rectified. The results of this study showed that anti-phase and full-wave rectified secondary corrugations ended up with reduction in pressure drop around 15 percent, however there will not be any significant changes in heat transfer. For in-phase secondary corrugations results have shown around 38 percent increase in pressure drop and 7 percent enhancement in heat transfer capacity.

1.3   Problem statement and objectives

There are many studies conducted so far on the subject. However there are still some gaps in the literature. There are few visualization studies exist, as far as our knowledge. The most popular ones are Dovic et al. (2009) , Focke and Knibbe (1985) and Gaiser and Kottke (1990) . These studies gives significant information about the flow structures inside the channel, however because of the difficulties of the experiments the range of Reynolds numbers are very low. Another issue is, the experiments does not change the parameters in detail. For instance, there is no information about how the plate width or length affects flow structures. Detailed analysis with different aspect ratios, angles, and corrugation patterns(chevron, washboard, herringbone) is required.

There are many numerical studies in literature using different models, geometries in literature. The effect of corrugation patterns, such as, herringbone, chevron, washboard, oblique washboard etc. is mentioned at very few articles and as far as the authors knowledge, it is not known how the flow structures change when the corrugation pattern changes or pressure drop and heat transfer. Another issue is most of the simulations used representative unitary cell and not the whole plate.

Some CPHE channels includes brazing points, especially those used at household heating systems and automotive applications. Gullapali and Sunden (2014) used channel with brazing points. In literature again the effect of these brazing points are not investigated. The influence might be great because of flow separation occuring at the wake of the brazes.

The transition from laminar to turbulence is a on going discussion in literature. The authors usually mentioned transition based on their flow visualizations or pressure drop and heat transfer data, however, there is no reliable information about it. Existing information from literature can be misleading when the parameters such as chevron angle, aspect ratio, corrugation pattern or corrugation profile (triangular, trapezoidal, sinusoidal etc.) changes.

Since the flow inside the CPHE channels are very complex, the lack of comprehensive experiment and numerical study which include flow visualization, pressure drop and heat transfer data considering wide range of Reynolds numbers, and wide value interval of such parameters like aspect ratio, chevron angle can be considered as a gap in knowledge.

So one of the important questions can be, how does the flow structures look like at high Reynolds numbers? Do they look same as in conducted flow visualizations so far(at low Reynolds) or they have some significant differences?

Another lack of knowledge is about transition. Where does the transition from laminar to turbulence happens? How does it respond to the changes in chevron angle, aspect ratio and plate dimensions(plate width, plate length)?

Again the effect of brazing point is not well known. How does brazing points affect the flow? How does the locations and orientations of brazing points affect the performance of the CPHE and flow?

This study will check whether transition can be inferred from friction factor trend lines. Again it seems flow changes in high Reynolds numbers in literature, the visual

experiments might show structures different than cross and helical flow. The brazing points might block the flow and change the flow directions.

The objectives of this thesis are mentioned below.

- Generating know-how on CPHEs by understanding the flow phenomena inside

- To observe flow structures at different Reynolds numbers and locations with the help of flow visualizations

- Determining the hydraulic character of the channel used by pressure drop measurements

- Conducting large eddy numerical simulations to analyze the flow behaviour inside the channel in detail

- Validating numerical simulations with flow visualizations and pressure drop measurements

CHAPTER II

METHODOLOGY

2.1 Experiments

2.1.1 Experimental setup

Experiments in this thesis can be grouped in three, which are pressure drop measurements and flow visualization experiments. The objective of pressure drop measurements was to determine the hydraulic characteristics of the single channel of a real CPHE used in household. Visualization experiments aim to demonstrate the flow structures inside a CPHE channel and to provide basic understanding of the flow phenomena. To be able to do so, two different visualization experiments have been conducted in this study, such as, aluminum-water mixture visualization and dye injection visualization, they provide global and local.

Pressure drop measurements were made in range of 100-2800 Reynolds number. Simply a pressure transducer was used to measure the pressure difference between the inlet and outlet port. A DAQ system provides the recorded data to experimenter.

For the first visualization, a mixture of aluminum particles and water was used. This method provides a global information about the flow structure through the channel. One can be able to analyze flow structures where their region of interest is at. The second visualization used dye injection method. In these experiments, dye was injected through pre-defined ports which placed at the bottom plate. Local flow structures can be analyzed by tracking the dye. However, the dye diffuses rapidly with increasing Reynolds number.
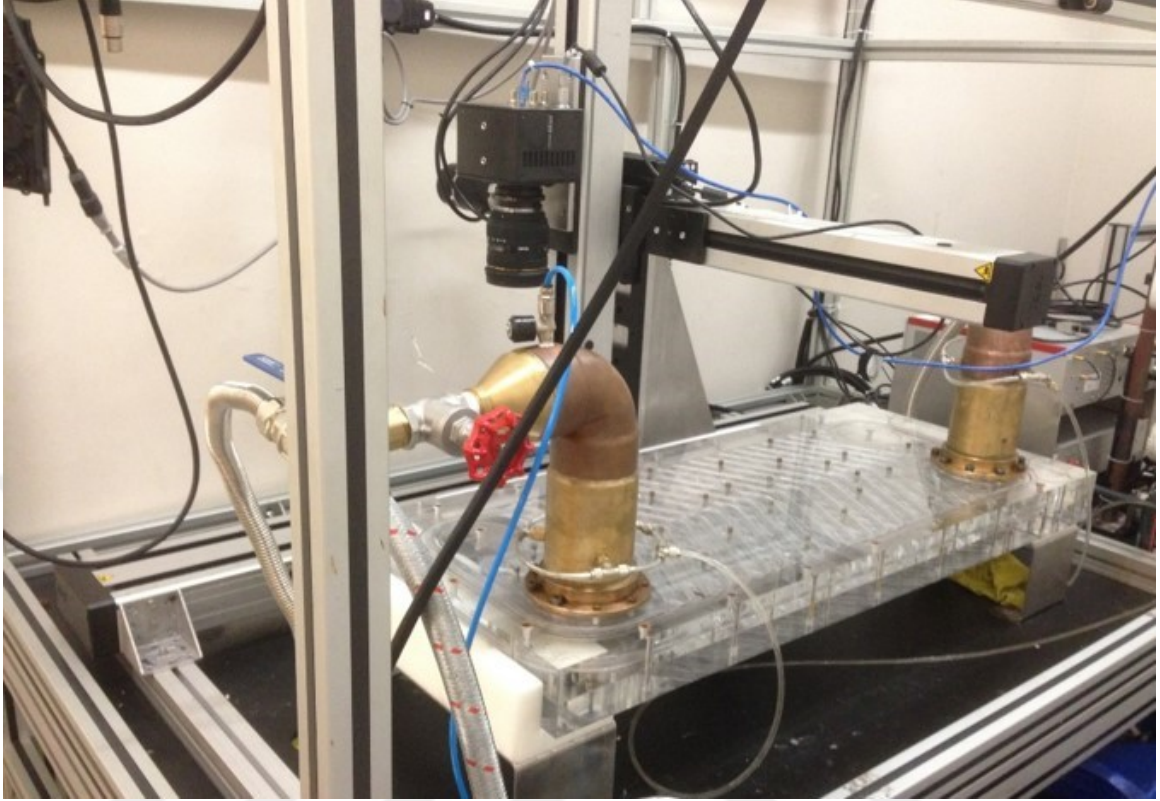
Figure 9: Experimental Setup

2.1.2   Instrumentation

The equipments used in the experiments are shown in Figure 12. Working fluid water is collected in a tank. While coriolis flowmeter and pressure transducer are recording data, the valve arranges flow rate provided to the CPHE channel. A Photron Fastcam is used for recording visual data and spotlight position and its power level defines the quality of the recorded visuals. For dye injection a syringe pump is used to pump dye to channel by ports.

Acrylic cell used is an upscaled version of the real model under dynamically similar conditions. It is for the ease of visualization experiments. The geometrical character-istics of the CPHE channel determines the performance. The geometrical parameter values are given in Figure 13. In experiments an ABB 2600T pressure transducer and a Siemens Coriolis flowmeter SITRANS FC410 was used.

Geometrical Parameters	
Hydraulic diameter (D_h)	0.00149 m
Channel width (L_w)	0.338 m
Port to port distance (L_v)	0.77 m
Chevron angle (β)	64°
Surface enlargement factor (φ)	1.14
Amplitude (a)	0.0085 m

Table 3: Geometrical parameters of Acrylic cell

Test Cases	Re						Re				
Experiments											
Visualization (Alumina)						Visualizations (Dye)					
Point1	276	553	1106	1416		Cross flow	276	553	1106	1416	2754
Point2	276	553	1106	1416		Helical flow	166	276	553	1106	1416
Point3	276	553	1106	1416		Wake					
Point4	276	553	1106	1416							
Point5	276	553	1106	1416							
Point6	276	553	1106	1416							
Point7	276	553	1106	1416							
Point8	276	553	1106	1416							
Point9	276	553	1106	1416							

Table 4: Visualization experiments with alumina

Test Cases	Re					
Numerical Simulations						
LES	276	553	1106	1660	2213	2767
K-epsilon	276	1660	2213	2767		

Table 5: Numerical simulation cases, LES and k-ϵ (used only in mixing study)

Test Cases	Q (l/min)
Experiments	
Pressure Drop Measurements	
Experiment 1	1.05; 2.114; 3.165; 4.004; 5.079; 6.0189; 6.982; 8.017; 9.366; 10.11; 11.45; 12.43; 13.12; 14.39; 15.26; 16.46; 17.45; 18.54; 19.43; 20.24; 21.36; 22.4; 23.55; 24.49; 25.47; 26.46
Experiment 2	1.05; 2.16; 3.18; 4.04; 5.22; 6.05; 7.01; 8.12; 9.07; 10.02; 11.22; 11.95; 13.02; 14.1; 15.07; 16.08; 17.01; 18.08; 19.02; 19.97; 21.02; 21.99; 23.01; 23.98; 25.03; 26.18
Experiment 3	1.05; 2.11; 3.18; 4.10; 5.05; 6.07; 7.08; 8.09; 9.27; 10.01; 11.04; 12.01; 13.13; 14.2; 15.01; 16.05; 17.03; 17.98; 19.07; 20.02; 21.00; 22.10; 23.04; 24.00; 25.02; 26.03; 26.72
Experiment 4	0.97; 2.11; 3.10; 4.19; 5.12; 6.21; 7.02; 8.04; 9.05; 10.08; 10.96; 12.05; 13.07; 14.06; 15.08; 16.03; 16.99; 18.07; 19.13; 19.97; 21.01; 22.05; 23.05; 24.02; 25.04; 26.16; 26.72

Table 6: Pressure drop measurements
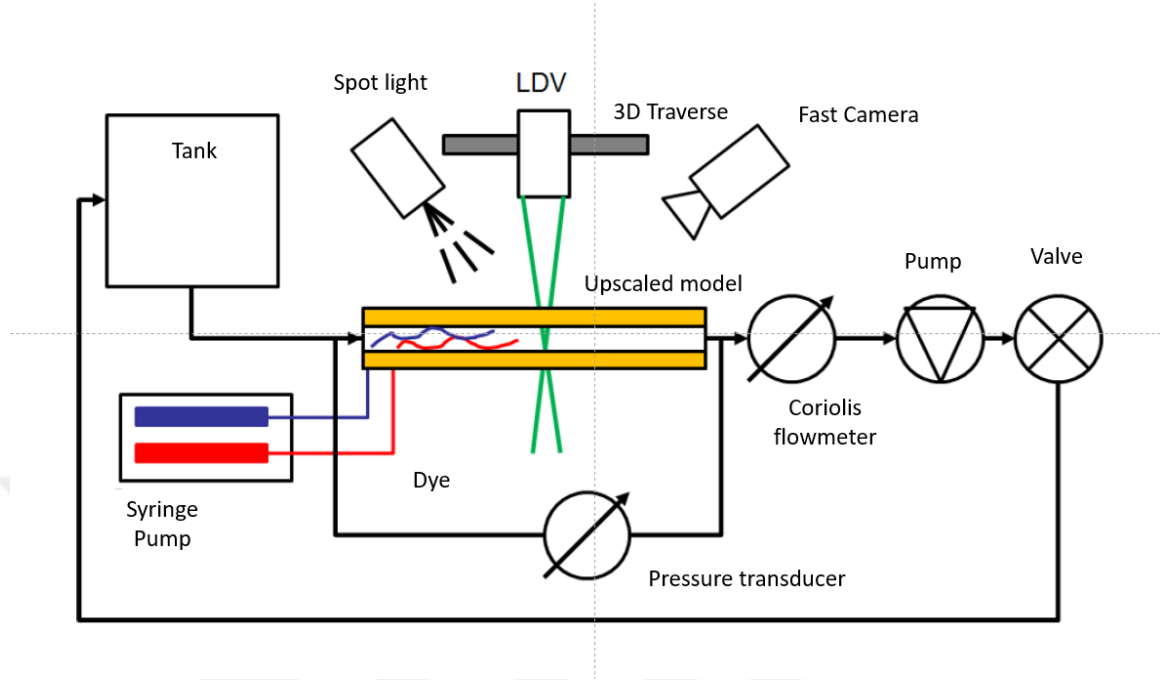
Figure 10: Schema of the Experimental Setup

2.2   Numerical Study

2.2.1   Numerical setup

Star CCM+ (version 13.04.011) industrial CFD software was used for the numerical estimations in this study.

LES solves large scales directly and smaller scales with modelling. Different than RANS models LES uses spatial filtering instead of averaging. In LES simulations solution variable α is decomposed into a filtered value ($\tilde{\alpha}$) and subgrid value (α').

$$\alpha = \tilde{\alpha} + \alpha' \tag{4}$$

Explicit filtering uses a Gaussian or box filter functions to discretize Navier-Stokes equations. As result filtering of a solution variable defined as:

$$\tilde{\alpha}(t,x) = \int\int\int_{-\infty}^{\infty} G(x - x', \triangle)\alpha(t, x')dx' \tag{5}$$

30

where $G(x, \triangle)$ characterized by filter width $(\triangle = (\triangle_x \triangle_y \triangle_z)^{1/3})$. When these decomposed solution variables inserted in Navier-Stokes equations.

$$\frac{\partial \rho}{\partial t} + \triangledown \cdot (\rho \tilde{\mathbf{v}}) = 0 \tag{6}$$

$$\frac{\partial}{\partial t}(\rho \tilde{\mathbf{v}}) + \triangledown \cdot \rho \tilde{\mathbf{v}} \otimes \tilde{\mathbf{v}} = - \triangledown \cdot (\mathbf{T} - \mathbf{T}_t) + f_b \tag{7}$$

where T_t is turbulent stress tensor, this term represents the subgrid scale stress in LES.

$$\mathbf{T}_t = 2\mu_t \mathbf{S} - \frac{2}{3}(\mu_t \triangledown \cdot \vec{\mathbf{v}} + \rho k)\mathbf{I} \tag{8}$$

$\tilde{\mathbf{v}}$: filtered velocity

$\mathbf{S}$: mean stress tensor $(\frac{1}{2}(\triangledown \bar{\mathbf{v}} - \triangledown \bar{\mathbf{v}}^T))$

ρ: density

k: subgrid scale turbulent kinetic energy

μ_t: subgrid scale turbulent viscosity

Subgrid scale turbulent viscosity equation is depending on the subgrid scale model you used. In WALE model definition of subgrid scale turbulent viscosity is as following

$$\mu_t = \rho \triangle^2 S_w \tag{9}$$

where again ρ is the density S_w is the deformation parameter and $\triangle$ is the grid filter width.

Grid filter width $(\triangle)$ is defined in terms of cell volume (V) as in equations below.

$$\triangle = \begin{cases} C_w V^{1/3} & \text{if length scale limit is not applied} \\ min(\kappa d, C_w V^{1/3}) & \text{if length scale limit is applied} \end{cases} \tag{10}$$

C_w is model coefficient. STAR CCM+ (version 13.04.011) user guide mentioned that the value of this model coefficient depends on the application. For channel flows as in our case 0.325 value is used for the C_w. κ is the von Karman constant.

31

S_w the deformation parameter in equation 9 defined as the following equation.

$$S_w = \frac{\mathbf{S}_d \div \mathbf{S}_d^{3/2}}{\mathbf{S}_d \div \mathbf{S}_d^{5/4} + \mathbf{S} \div \mathbf{S}^{5/2}} \tag{11}$$

$\mathbf{S}_d$ is defined as

$$\mathbf{S}_d = \frac{1}{2} \left[\triangledown \mathbf{v} \cdot \triangledown \mathbf{v} + (\triangledown \mathbf{v} \cdot \triangledown \mathbf{v})^T \right] - \frac{1}{3} (\triangledown \mathbf{v} \cdot \triangledown \mathbf{v}) \mathbf{I} \tag{12}$$

The physical domain is one CPHE channel with inlet and outlet as presented in Figure 11. The main difference between the channel geometry in Figure 11 and common CPHE geometry, that used in previous studies, is brazing points which affect the flow significantly.

For meshing polyhedral mesher and prism layer mesher options were used for pre-processing.

Around 4 million cells were used in order to get accurate results. The mesh scenes are presented in Figure 12(a,b). The LES model was used for all simulations except for the mixing study. k-ϵ model was used for mixing study. Large eddy simulation(LES) model and Wall-Adapting Local-Eddy Viscosity(WALE) Subgrid Scale used for modeling turbulence. The detailed information of the model can be found in Nicoud and Ducros (1999) . Figure 12(c) shows the y+ values on surface. Maximum y+ value is around 7, which is limited to a small region next to exit. Here it is assumed that wall effect is sufficiently resolved. Figure 13 exhibits the mesh sensitivity, after 4 million elements, friction factor increased 2 percent when Re = 2767 and increased 4 percent when Re=276.

In LES, turbulent implicit unsteady physics used. Segregated flow option, is used in our three dimensional simulations. As mentioned below WALE subgrid scale model is selected, since it is the most appropriate model, especially narrow and complex geometries as in our case. All y+ treatment option is used which uses hybrid y+ model details of the model is represented in STARCCM+ (version 13.04.011) user

guide. Time step defined as 0.01 second. Simulation cases are run minimum up to 30 seconds. At the highest Reynolds number used in simulations, one pass takes around 7 seconds and minimum Reynolds number it takes around 70 seconds.
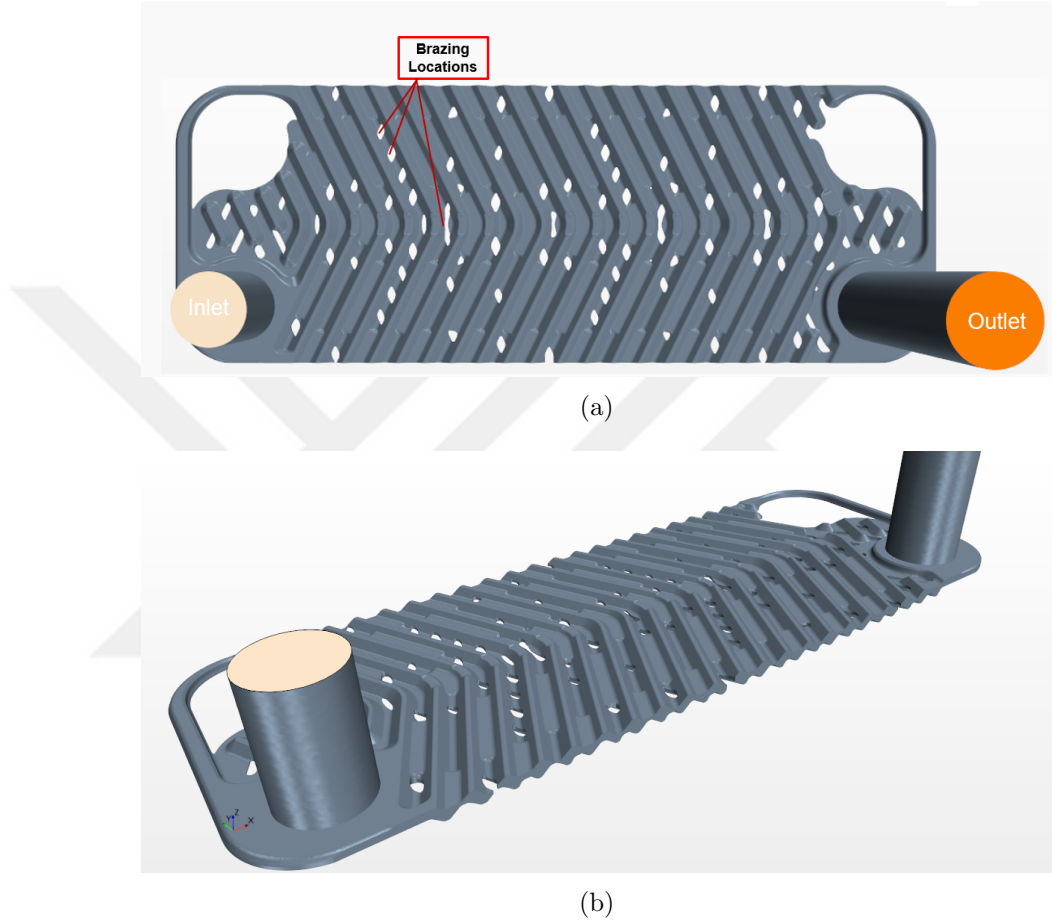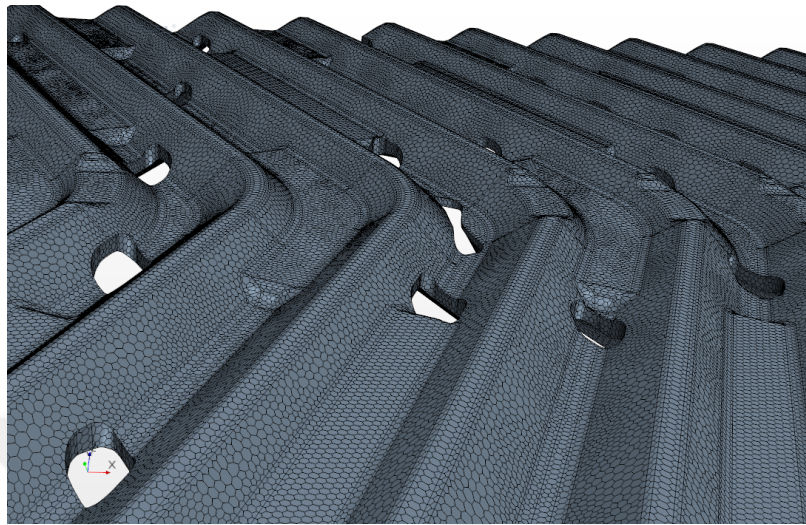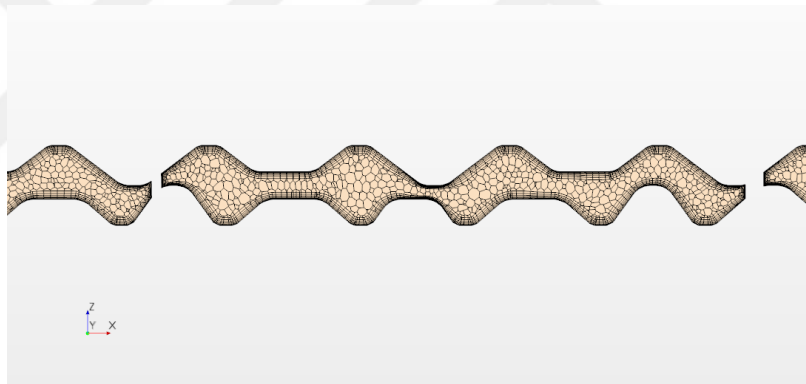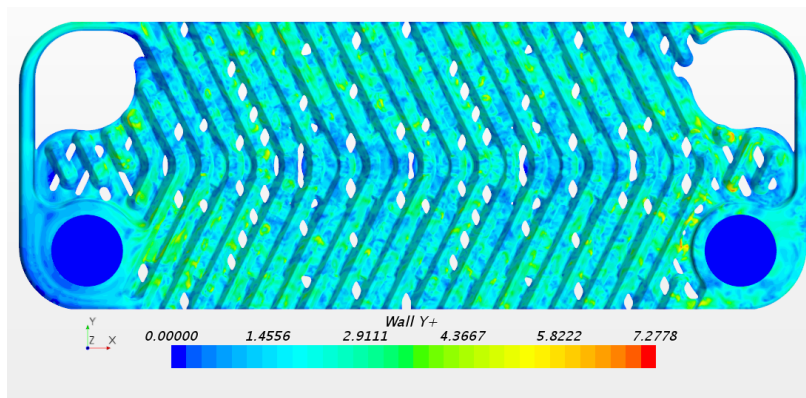

(a)

(b)

Figure 11: Schema of the Experimental Setup

(a)

(b)

(c)

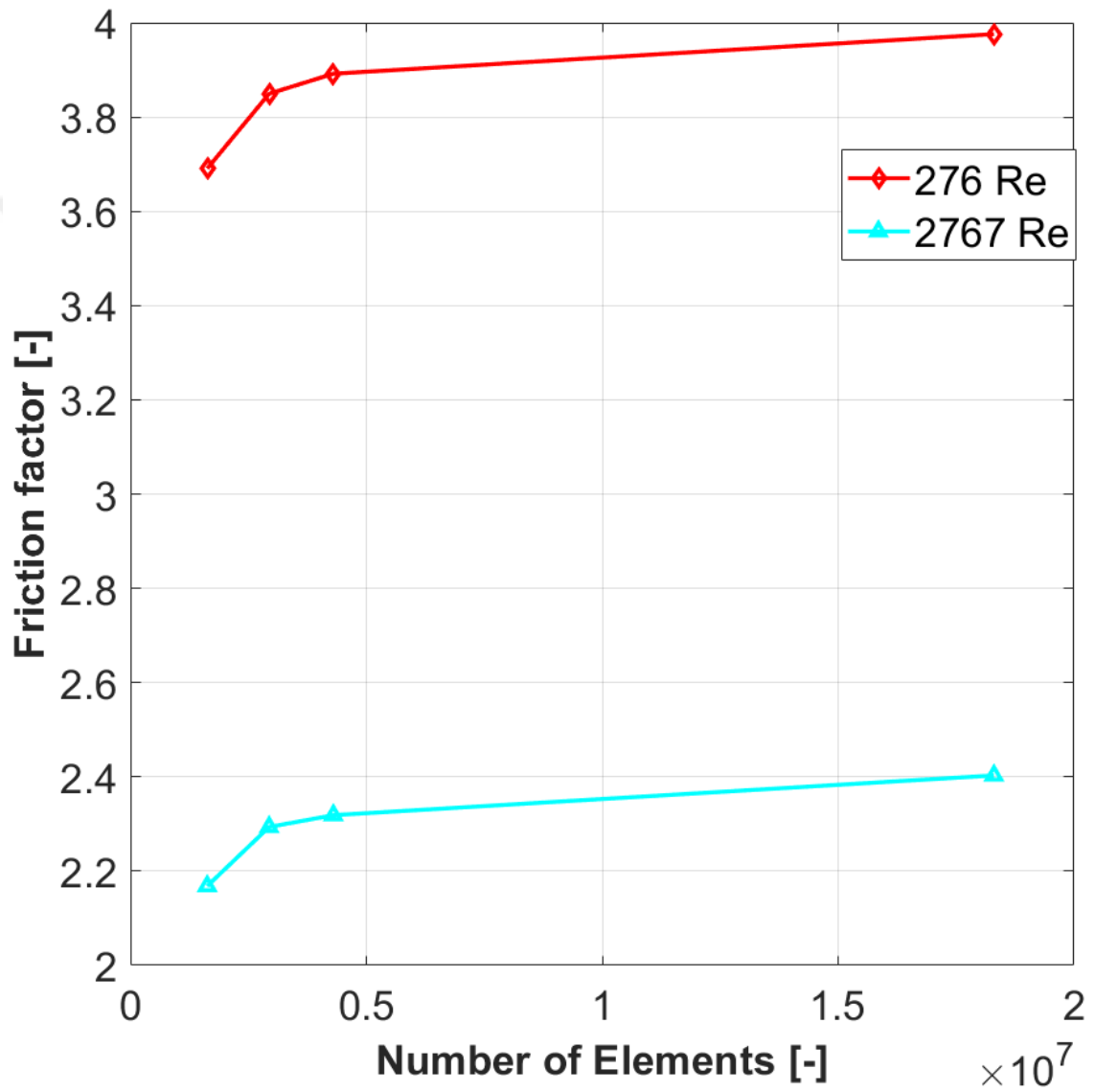**Figure 12:** Meshes on (a)surface of geometry, (b) section; (c) y+ value at surface

34

Figure 13: Mesh Sensitivity at 2767 Re (cyan) and 276 Re (red)

CHAPTER III

EXPERIMENTAL RESULTS

3.1 Pressure drop measurements

Friction factor versus Reynolds number graph is shown in Figure 15. The experiments are repeated several times, different experiments are shown with different colors in this Figure. Reynolds number and friction factors defined as Kakac and Liu (2002)

$$Re = (\frac{G_c \times D_h}{\mu}) \tag{13}$$

$$f = 2\Delta P A_c^2 \frac{D_h}{L_v} \frac{\rho}{\dot{m}^2} \tag{14}$$

where hydraulic diameter (D_h) and mass velocity (G_c) is

$$D_h = (2 \times a)/\varphi \tag{15}$$

$$G_c = \frac{\dot{m}}{a \times L_w} \tag{16}$$

In equation 4, μ represents dynamic viscosity of the working fluid and $\dot{m}$, φ, b, L_w corresponds mass flow rate, surface enlargement factor, corrugation depth, channel width respectively. In equation 5, while L_v is the port to port distance, A_c represents the cross sectional area of the CPHE channel.

Friction factor defined in Eq. (5) and Re defined at Eq (4). In Figure 15 at low Re the friction factors decreased drastically with increasing Re. There is a significant change observed around Re $\cong$ 500 in Figure 15 which also corresponds to flow rates where the flow structures became smaller identified by visualization experiments.

36
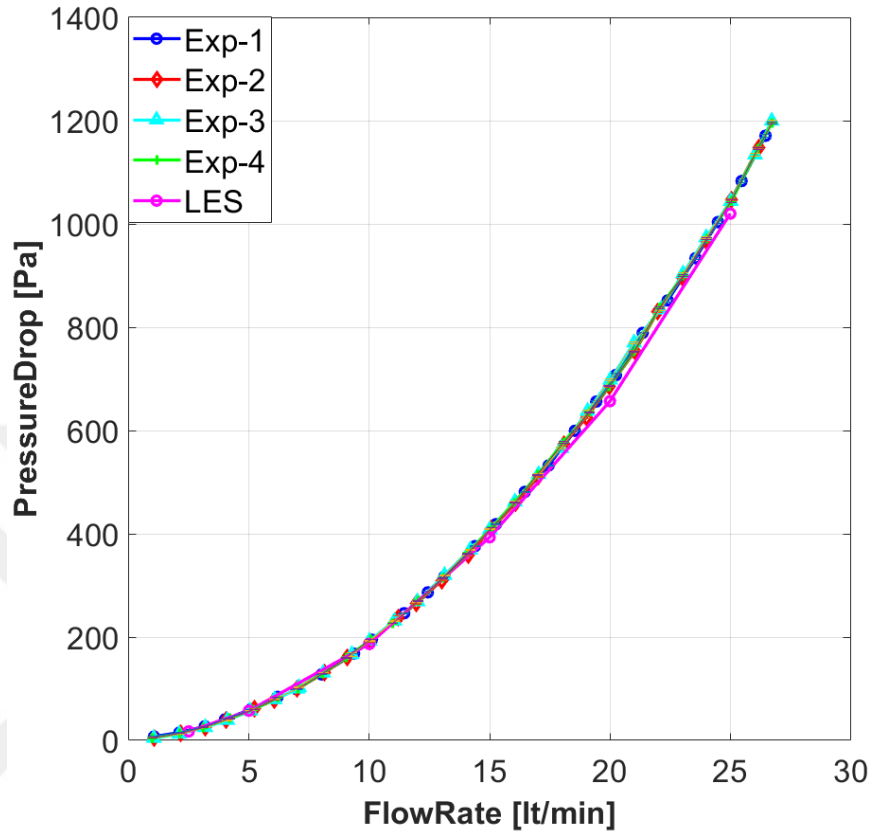
Figure 14: Pressure drop vs. Flow rate

Friction factor vs. Reynolds number plot cannot be represented by a single curve fit. Two trend lines must be used as can be seen from Figure 15 These trend lines, as negative power of Re, had intersection around Re $\cong$ 500. It can be said that there should be a transition region around intersection point of trend lines.

In experiments, measurement time is defined based on statistical error. Statistical error is a function of number of independent samples. At low flow rates, necessary measurement time for a required number of independent samples increases. In other words, to keep the statistical error at required level, the measurement times are longer at low flow rates in experiments. The governing equations used while calculating statistical friction factor error represented below.

$$\bar{V}_i = \bar{\dot{Q}}_i/A \tag{17}$$

In equation 17, average flow velocities calculated from the measured volumetric flow rate. For each data point in Figure 15, first average flow rate throughout the measurement calculated. For each flow rate and pressure drop measurement, the data acquisition records to data in every second. To calculate the average flow velocity, $\bar{V}_i$, the average flow rate was divided by average cross sectional area, A.

$$\tau_{flow,i} = L/\bar{V}_i \tag{18}$$

$\tau_{flow,i}$ defined as length, L, divided by the average flow velocity, $\bar{V}_i$. This value represents, how much time it takes for a pass.

$$N_i = t_i/\tau_{flow,i} \tag{19}$$

N_i represents the number of independent samples. t_i is the measurement time, simply amount of time for each measurement for each flow rate. The statistical error for friction factor, ϵ_f calculated, where $stdev_{f,i}$ represents the standard deviation of friction factor in time for flow rate (i). These statistical errors are represented in Figure 15 as error bars.

$$\epsilon_f = 2stdev_{f,i}/\sqrt{N_i} \tag{20}$$

3.2 Flow Visualization Experiments

One of the visualization method used was visualization with aluminum flitter and water mixture. This method provides a global information about the flow phenomena, however it is not possible to represent this data with frames. Instead of describing phenomena with figures, the observations made through the experiments will be mentioned in this paragraph. The channel geometry can be divided in to three which are
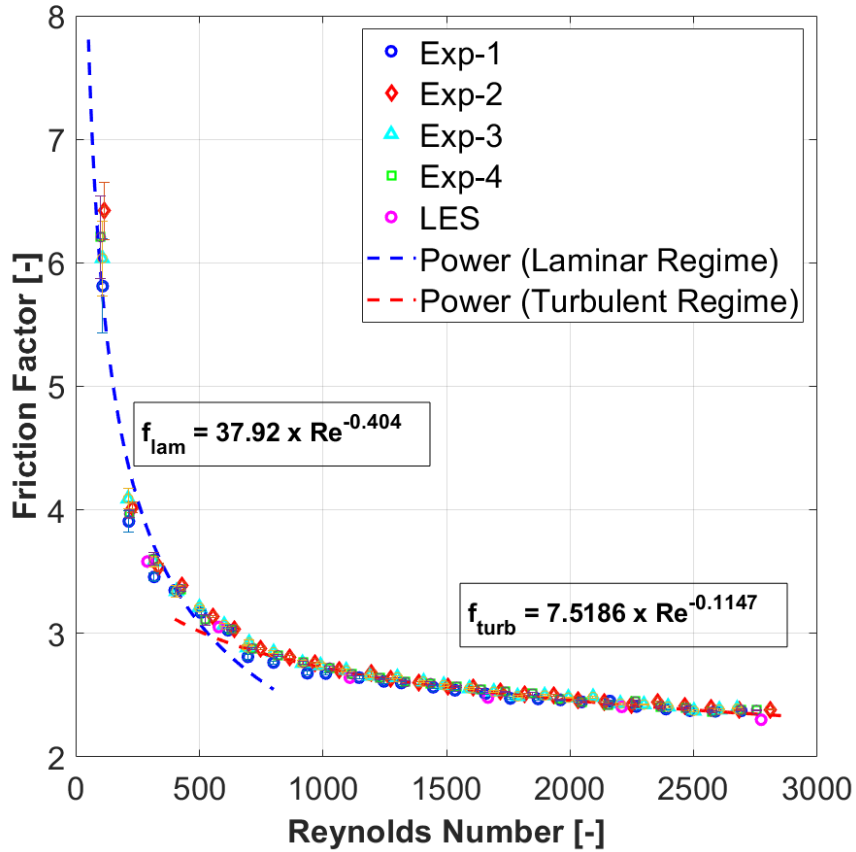
Figure 15: Friction factor vs. Flow rate

inlet distribution region, core region and outlet distribution region. Inside inlet distribution region, significant back flows observed, especially in front of brazing points around the inlet port. Inside inlet distribution region, small eddies can be observed in port side around point 5, while no eddies on the other side around point 4 when Re = 276. The reason might be the non-uniform distribution of flow which ended up with velocity differences at different sides of the channel. There is a significant change in flow structures in between 276 Re and 553 Re. When Re = 276 the structures are bigger and direction of the flow can be observed, in other words the flow is ordered. However, at Re=553 flow structures are smaller and there is great increase in small eddies. At higher Reynolds numbers, it becomes harder to make comparison because there is no observable changes in flow phenomena. Also, the differences between

Number of independent samples(N)	Re									
	108	214	317	399	505	615	696	790	936	1011
N_exp1	0.74	1.09	1.94	1.69	2.42	2.64	3.07	3.59	7.31	8.98
	112	229	336	427	553	641	747	865	966	1067
N_exp2	4.55	8.35	7.67	6.66	4.31	2.67	2.97	3.68	5.60	4.41
	106	211	316	406	499	600	693	701	800	917
N_exp3	10.99	8.87	8.71	14.48	15.29	8.35	15.29	8.35	3.93	3.90
	99	215	314	424	524	629	712	818	921	1027
N_exp4	5.36	17.12	13.46	20.97	19.79	20.53	4.81	3.47	15.02	4.89

Table 7: Number of independent samples in experiments
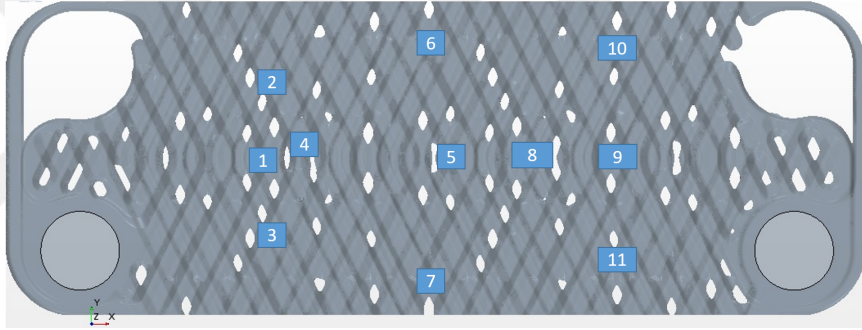
Figure 16: Investigation areas for Aluminum-water visualization experiment

point4 and point5 region decreases with increasing Reynolds numbers. Inside core region, different flow structures at different sides as in inlet distribution region cannot be observed. With increasing Reynolds number structures getting smaller. Again there is significant change from Re=275 to Re=553. Flow in corrugation direction seems to increase and swirls are more intense with increasing Reynolds numbers.

Visualizations from the dye injection experiment are represented in Figure 18 and Figure 19 at Re = 276. When it is compared to previous visualization experiments, the operating conditions and plate geometry is different from them. These differences are chevron angle, the chevron corrugation type, Re range. For instance Focke and Knibbe [Focke and Knibbe, 1986] observe a flow at 45 degree chevron angle CPHE
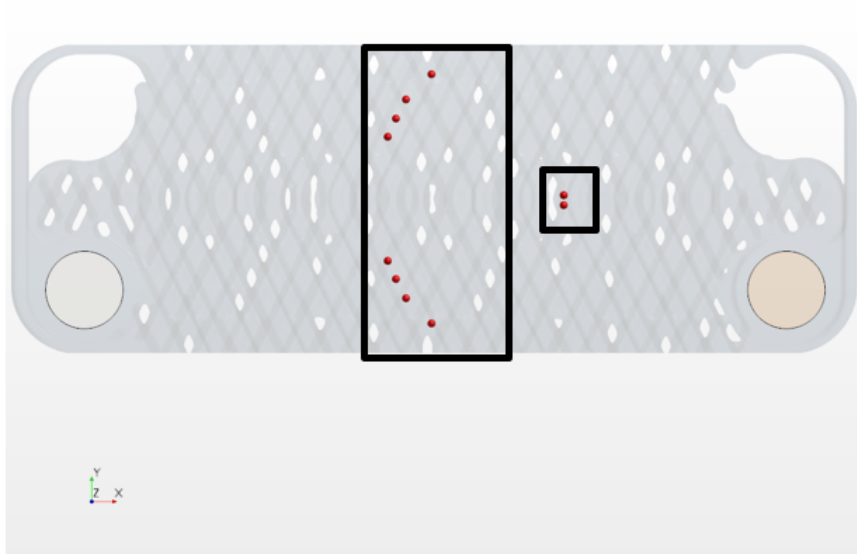
Figure 17: Dye injection ports

which follows the corrugation until it reaches the wall. This existence of pure cross flow is related to chevron angle they used and diffusion of dye is very low because of the low Reynolds numbers. The chevron angle is a property which increases the presence of helical flows significantly. The different chevron angles and the brazing point locations, that included in the test section, block the flow and forces it to change its direction. These are the main reasons that cause a different flow inside the CPHE channel of the present study.

From Figure 18 one can observe that the dye injected from the ports closest to side walls, flows inside the corrugation. Dye injected from ports close to the center is unsteady and it follows corrugation for an instant, then change its direction and flows longitudinally at another instant. At the left side of Figure 18, one can observe that flow is more likely to flow in longitudinal direction, while at the right side the flow follows corrugation direction more dominantly.

Figure 19 shows that the dye injected from ports next to side walls. It can be seen that the dye follows the corrugation until it reaches to side walls. Then it shows a helical flow behavior and penetrates one corrugation, this time it follows the opposite
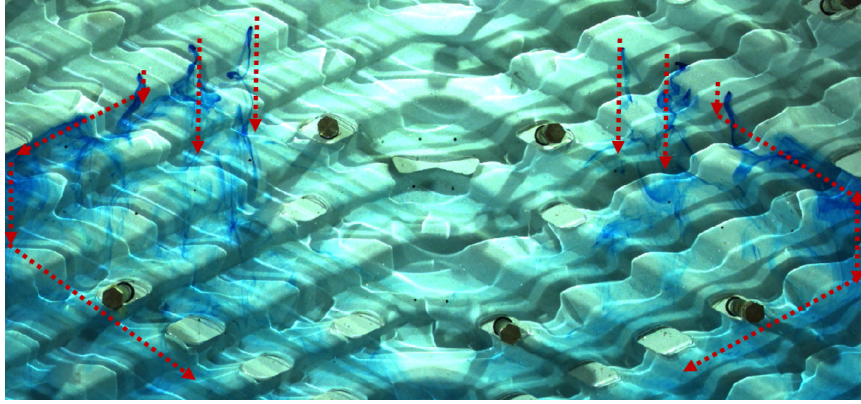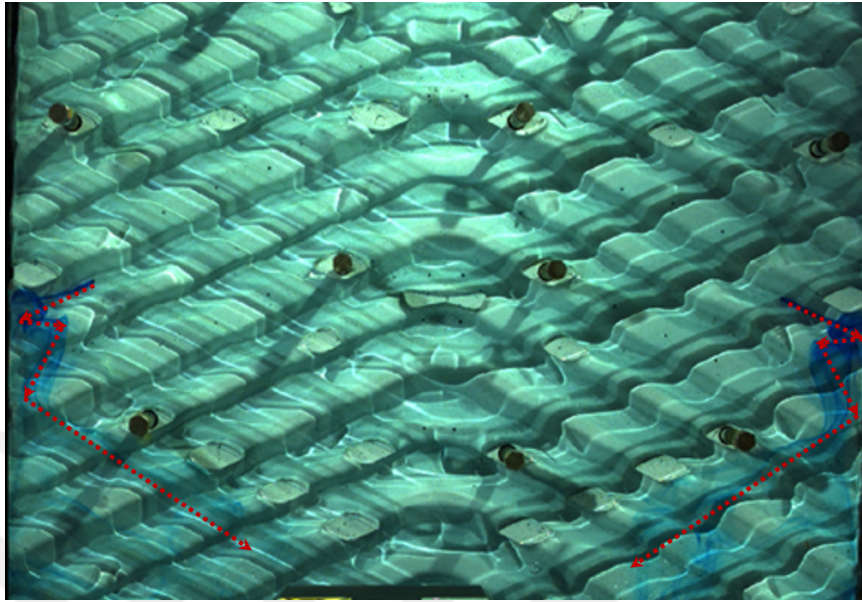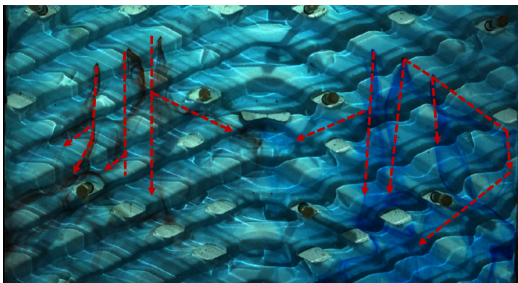
Figure 18: Visualization with dye injection at Re=276, helical flow corrugation.

The dye injection along an edge of a cross-corrugation is represented in Figure 20 at different Reynolds numbers. At high Reynolds numbers it becomes harder the visualize the flow with dye injection method, however at low Reynolds numbers the flow path can be observed as seen in Figure 20(a) and Figure 20(b). From Figure 20(a) one can observe very less dye flows in the corrugation direction, longitudinal direction flow is dominant at this Reynolds number. While the left side of the channel has more wavy flow in other words direction changes very often, right side of Figure 26(a) has no velocity direction changes with time. This part of the channel is steady in this case. Figure 20(b) has the same operating conditions with Figure 18. In Figure 20(c,d) dye diffused immediately in flow. However, it can be observed that flow structures getting smaller with increasing Reynolds number. Fluctuations of velocity direction are increasing at higher Reynolds numbers.It is hard to understand the exact phenomena with a single frame because of the direction of flow changes with time, especially for high Reynolds numbers.

Figure 19: Visualization with dye injection at Re=276, cross

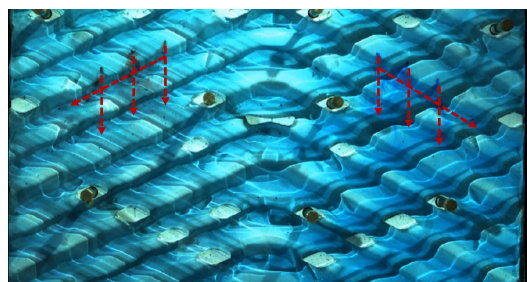(a)
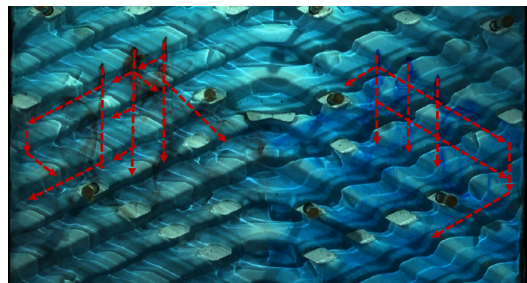
(b)
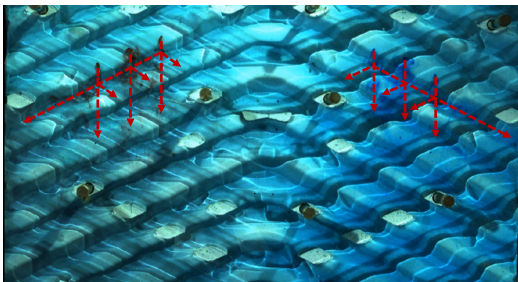
(c)

(d)

Figure 20: Visualization with dye injection (a) 1.5 lt/min- Re =166, (b) 2.5 lt/min-Re = 276, (c) 5 lt/min- Re = 553, (d) 10 lt/min- Re =1106

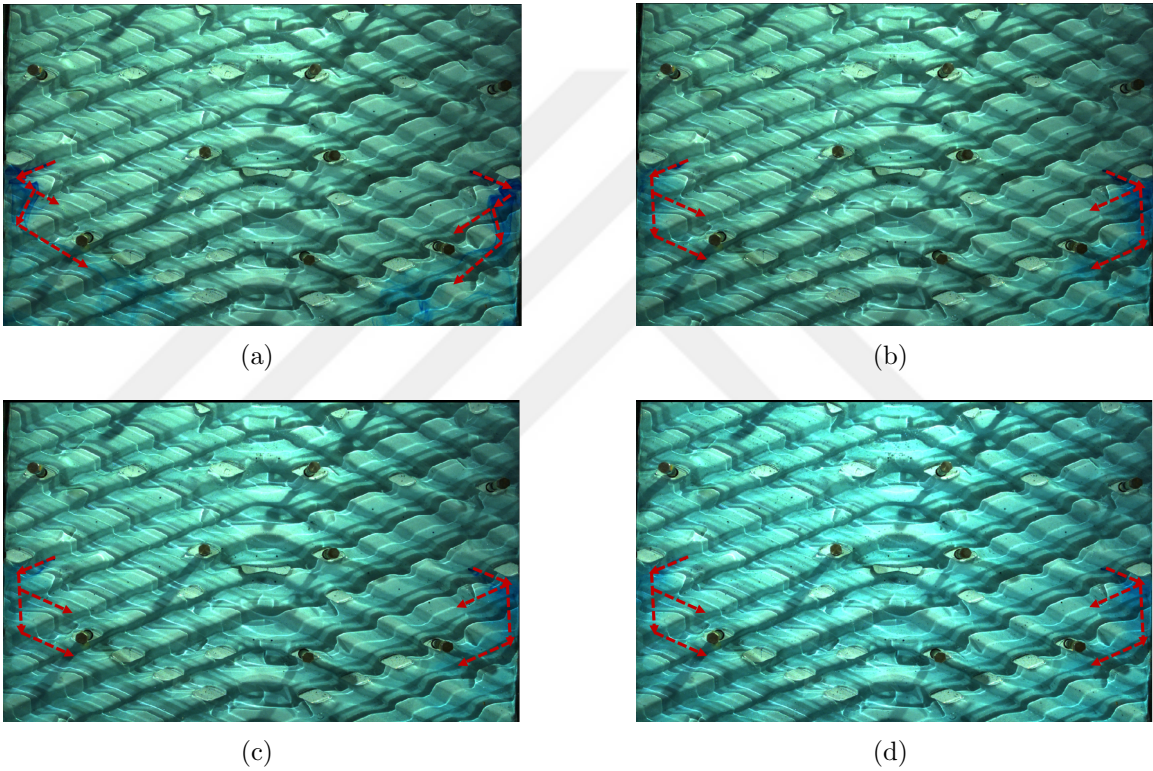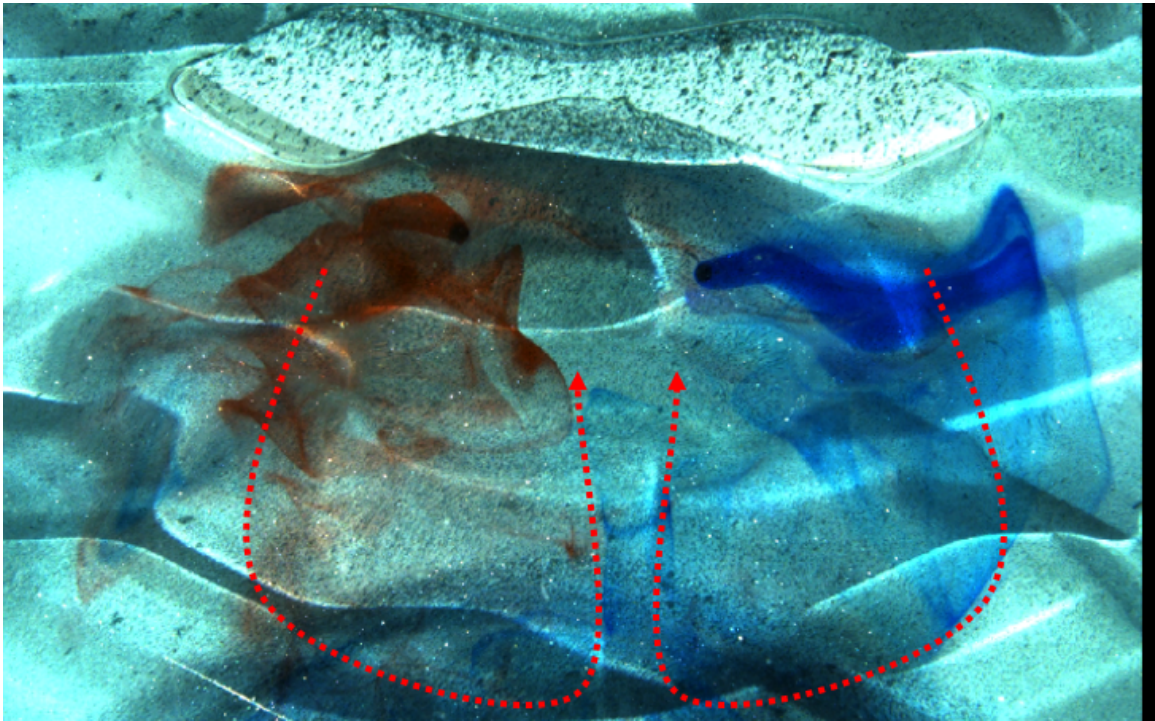**Figure 21:** Visualization with dye injection (a) Re =276, (b) Re = 553, (c) Re = 1106, (d) Re =1416

Figure 22: Wake behind brazing point

CHAPTER IV

NUMERICAL RESULTS

4.1 Pressure drop and Friction factor estimations

Figure 15 exhibits that maximum deviation of LES friction factor estimation is 5 percent from the experimental results which is less than some previous works e.g. Sarraf et al. (2015) .

4.2 Large Eddy Simulations

Figure 23 to 26 are demonstrating the streamlines which are started from identical positions of ports in Figure 7. Only Figure 23 can be compared with dye experiments, because of the fact that dye diffuses in channel flow rapidly with increasing flow rates.

In Figure 27 (a,b,c,d,e,f) comparison of velocity fields made at Re = 276 and Re = 2768. Velocity fields described by plane 1, plane 2, plane 3. Plane 1 is located at the mid-height of upper corrugation, plane2 is at the mid-height of the channel and plane 3 is located at the middle of lower corrugation.

Plane 2 is in the middle of the channel, the Figure 27 (c,d) shows that flow is directed towards outlet. While Figure 27 (c) has straight flow direction towards outlet, Figure 27 (d) has more flow direction changes in the field, described as wavy structures in the figure.

The numerical visualization at Figure 31 exhibits at the inlet and outlet regions of the CPHEs wall shear stresses are greater than the rest of the channel. The shear stresses seem symmetrical except the inlet and outlet regions. Another observation is higher shear stress occurred at the top. Behind the brazing points, where wake structures occur, the shear stress is very low compared to rest because of the lower
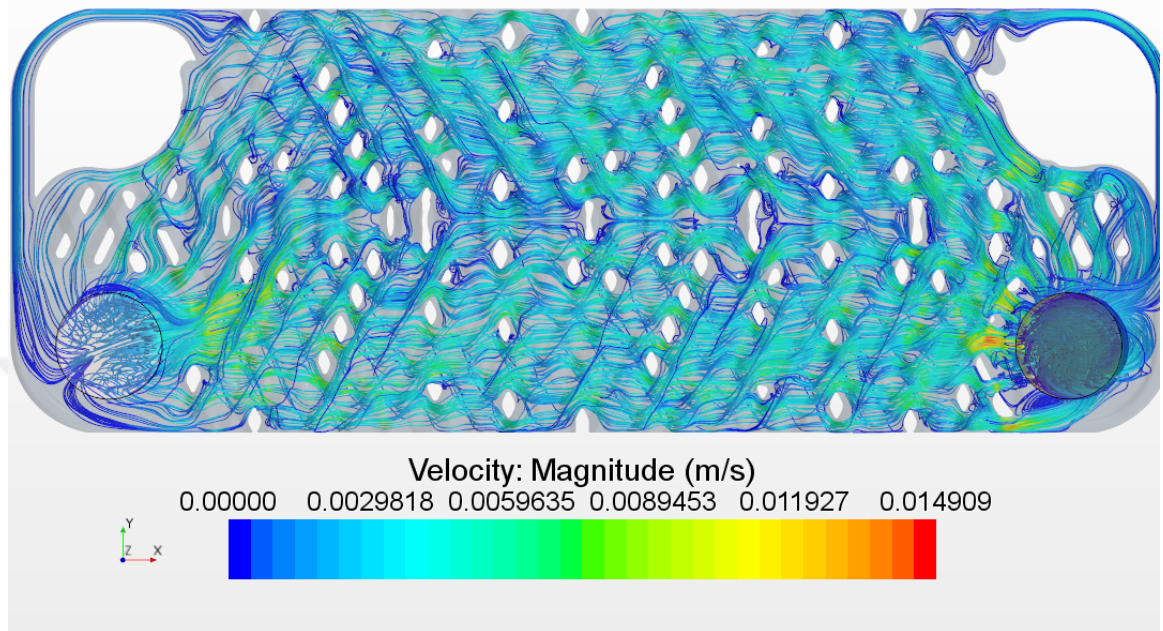
Figure 23: Global streamlines at Re =70

speeds in recirculating wake.

Comparison of dye visualization and LES streamlines behind the brazing points are represented in Figure 29. In Figure 29 (a) it can be observed that the blue and red dye, first flow inside bottom corrugation direction. Flow coming inside the the top corrugation interacts with the dye. As a result of this interaction, while some of the dye continues to following bottom corrugation, some of it turns to flow at the top corrugation. The blue and red dye in Figure 29 (a) which are following top corrugation meet at the center. Between the point that dyes come across and brazing is the separated region where both dyes recirculate.

4.2.1 Laminar to turbulent transition

Transition point inside CPHE is an open discussion in literature. Some authors gives critical Reynolds numbers usually based on visualization studies. However, since
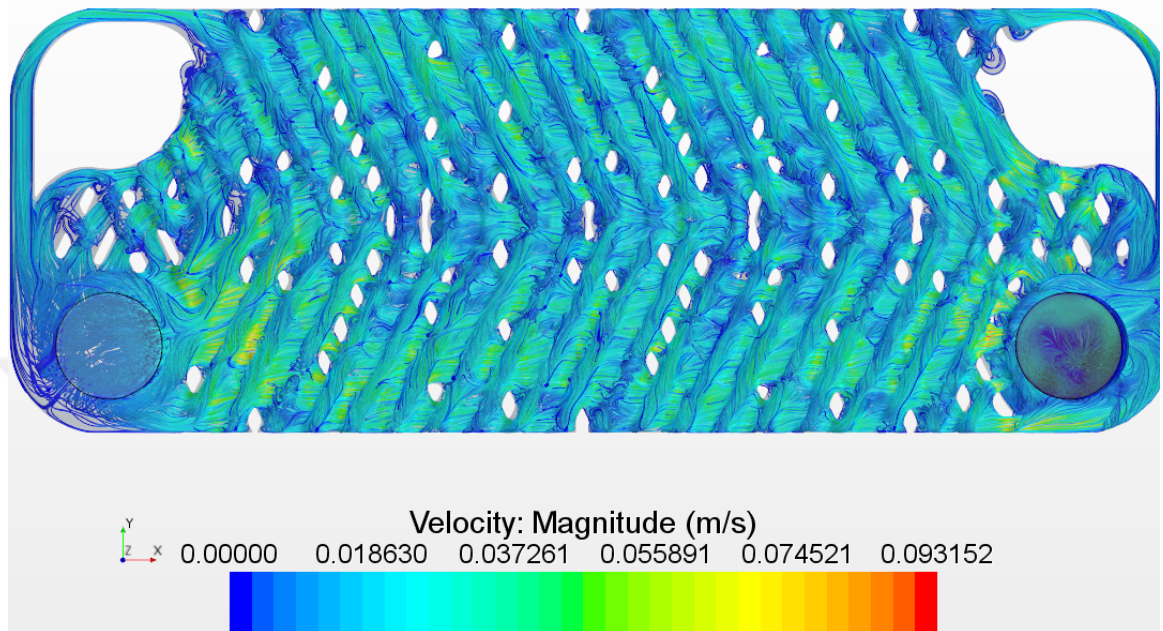
Figure 24: Global streamlines at Re = 276

there is no sharp transition occuring inside channel, it is difficult to determine where exactly transition begins. In this subsection, some points defined on CPHE channel and velocity magnitudes on these probes analyzed. Figure 30 exhibits the location of probes. For every single location there are three probes which have different depths as can be seen in Figure 30(b). Using velocity magnitudes on these points, a power spectral density graph was made in Figure 31. In the PSD figure, it can be seen how the energy distributed to frequencies. From Re = 265 to Re = 275 distribution of the energy changes significantly. First the amplitudes increase for each frequency. Second, a turbulent energy cascade appear for Re larger than 275. The spectrum lower than this value exhibit energy on distinct frequencies. At higher Res than 275, with the increasing frequency, the power value decreases however does not fluctuate as in low Res. This is characteristic at high Res is a sign of turbulence. Figure 31(b) was normalized by mean square of velocity fluctuations. Moreover, turbulent
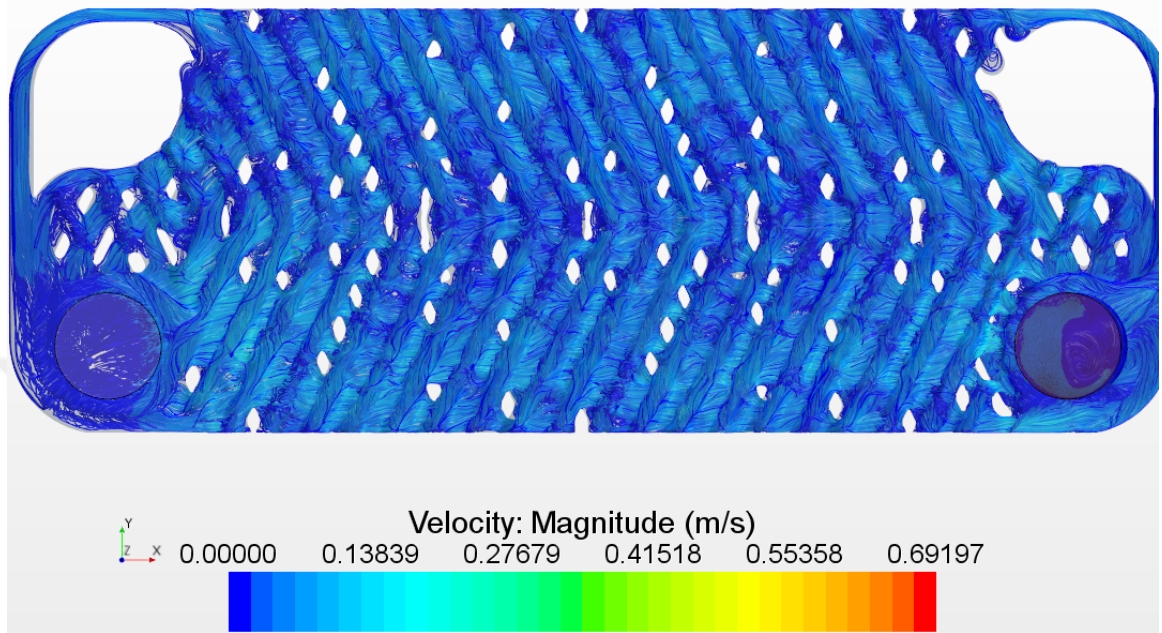
48

Figure 25: Global streamlines at Re = 553

intensities was inspected. Turbulent intensity table, and plot can be seen in Figure 32,33. Where turbulent intensity defined as ratio of root mean square of velocity fluctuations to average velocity.

$$Turbulent intensity = \frac{rms(\mathbf{v}_{fluc})}{\bar{\mathbf{v}}} \tag{21}$$

There was a significant change observed between Re = 265 and Re = 275 on both ports.

4.3   Mixing

Physics modelling in Mixing simulations, includes steady, k-ϵ turbulence model. RANS equations are selected. Additionally, in these simulations passive scalar option is used. There is no effect of passive scalars on the flow. This makes the option appropriate for investigating mixing inside the channel. The transport equation for the passive
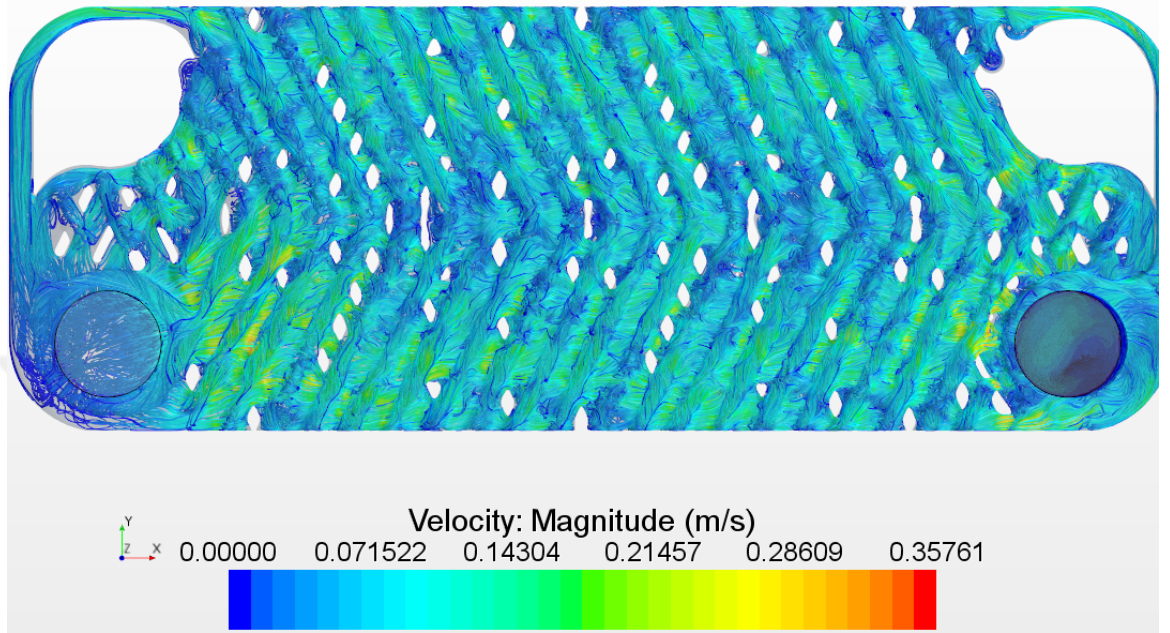
Figure 26: Global streamlines at Re = 1106

scalar component ϕ_j is as equation below.

$$\frac{\partial}{\partial t} \int_V \rho\phi_i \cdot dV + \oint_A \rho\phi_i \mathbf{v} \cdot d\mathbf{a} + \int_V S_{\phi_i} dV = \oint_A \mathbf{j}_i \cdot d\mathbf{a} + \int_V S_{\phi_i} dV \qquad (22)$$

where i represents the component index, j_i has shown the diffusion flux. S_{ϕ_i} is the passive scalar source term and ϕ_i assumed to be positive definite. Also the linear eddy diffusivity model for passive scalar is as shown.

$$\mathbf{j}_i = \left(\frac{\mu}{\sigma} + \frac{\mu_t}{\sigma_t} \right) \triangledown \phi_i \qquad (23)$$

where μ and μ_t are viscosity and turbulent viscosity, respectively σ and σ_t are Schmidt number and turbulent Schmidt number. $\mathbf{j}_i$ represented the diffusion flux.

Mixing inside the channel is analyzed through defining two passive scalar flux from upper and lower corrugations between 0.35-0.55 meters in x-direction, the entrance regions of passive scalar showed in figure 34. Schmidt number and turbulent Schmidt
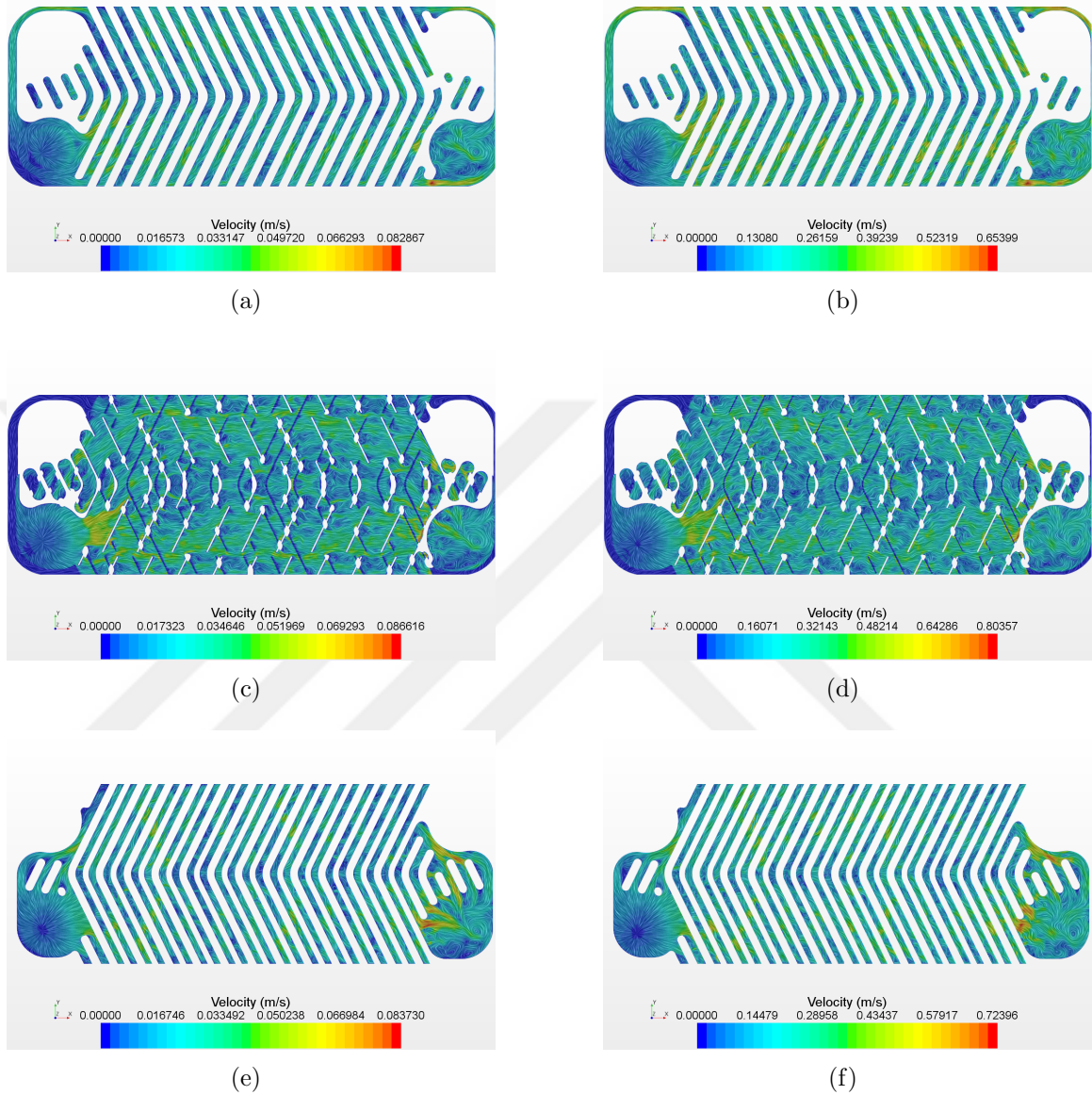
50

Figure 27: Visualization (a,c,e) velocity field at Re=276 on plane 1,2,3 respectively; (b,d,f) velocity field at Re=2768 on plane 1,2,3 respectively

number defined as 3.628 and 0.9, respectively and the passive scalar flux given is 10 $kg/m^2 - s$ from bottom (only S_B) and from top (only S_A) Mixing is normalized with the maximum value in fluid region mixing. Figure 35 presents the surface average of normalized mixing of cross-sections located at distances in x-coordinate. The
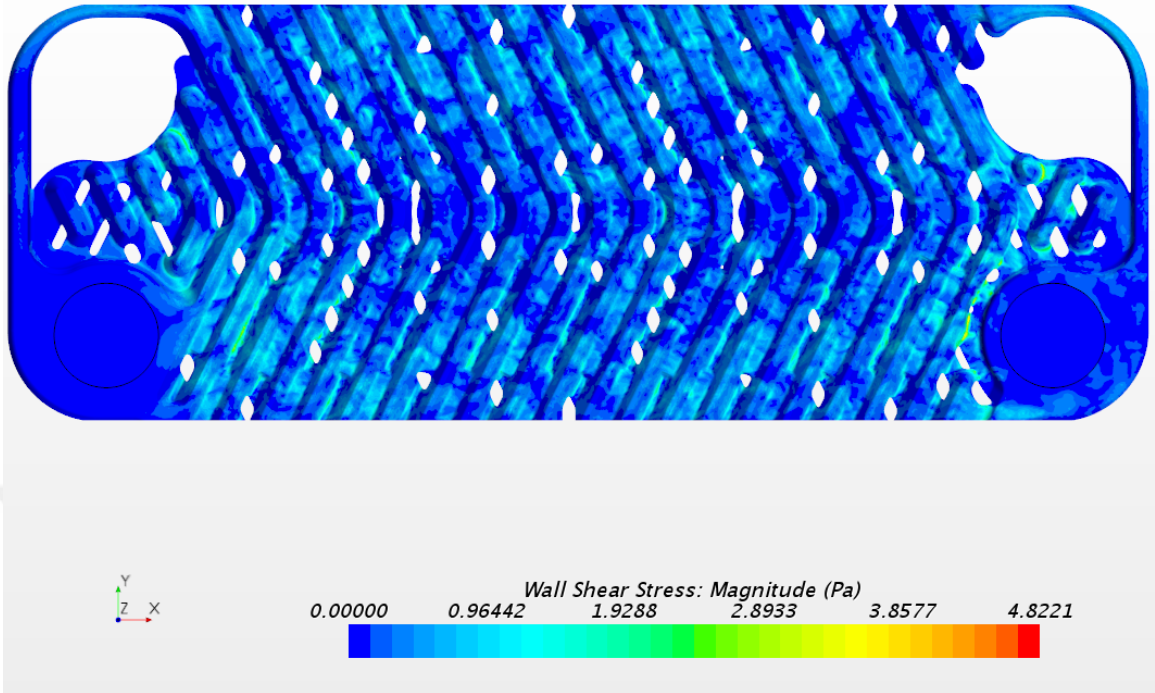
(a)
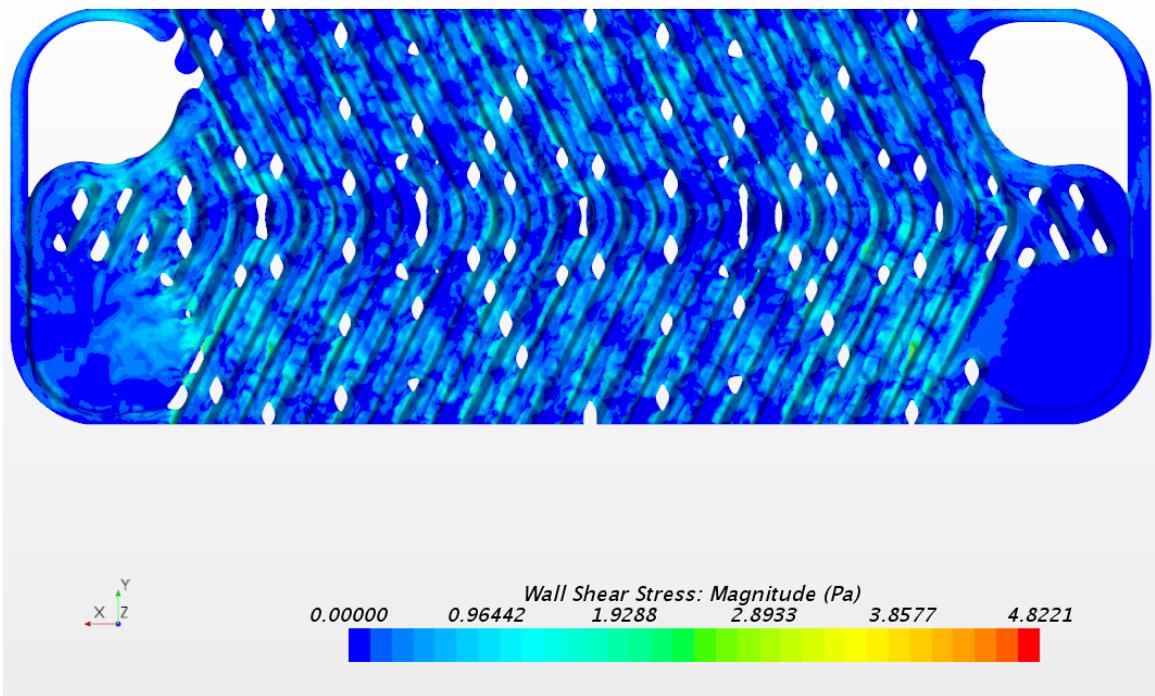
(b)

Figure 28: Wall shear stress on (a) top , (b) bottom surface
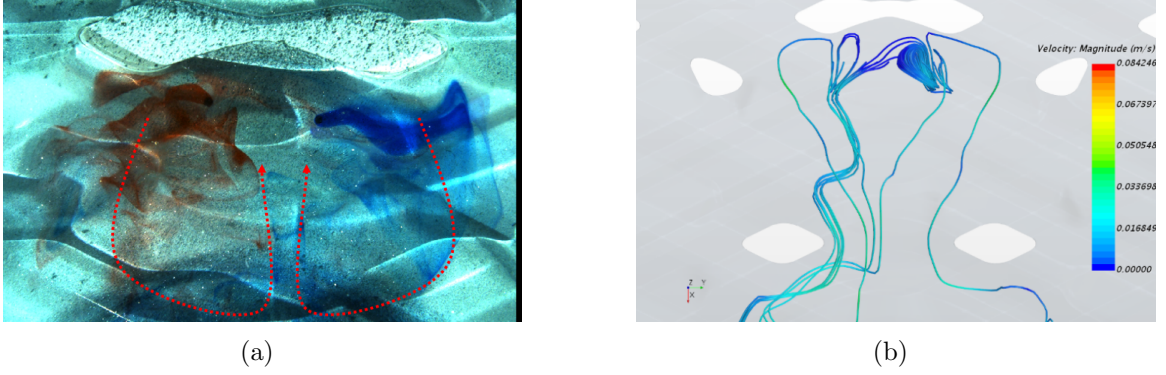
<center>(a)   (b)</center>

Figure 29: (a)Wakes behind brazing points at 2.5 lt/min- Re = 276, (b)LES stream-
lines from identical points in dye injection experiment at 2.5 lt/min- Re = 276

normalized mixing is defined as in equation below.

$$\textbf{Normalized mixing} = \frac{S_A S_B}{S_{A,max} S_{b,max}} \tag{24}$$

where S_A is for Scalar A values, S_B is for Scalar B values. They are normalized by
the highest values in fluid domain reported. Normalized mixing values increase with
high Reynolds numbers. In Figure 36 one is able to see the local normalized mixing
values inside fluid domain. These values are shown with threshold option in STAR
CCM+, threshold shows the cells, where defined scalar value is inside the interval
given. Figure 36 exhibits two different mixing ranges 0.8-1.00 and 1.01-5. From the
figures, the asymmetric mixing can be observed, since high mixing values mostly take
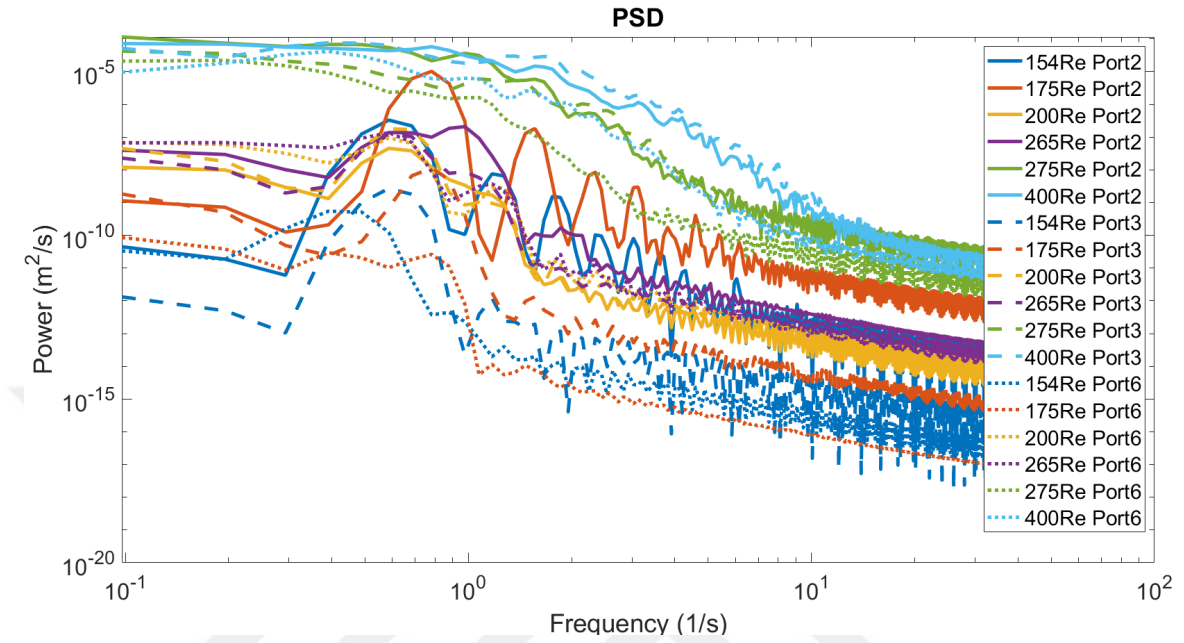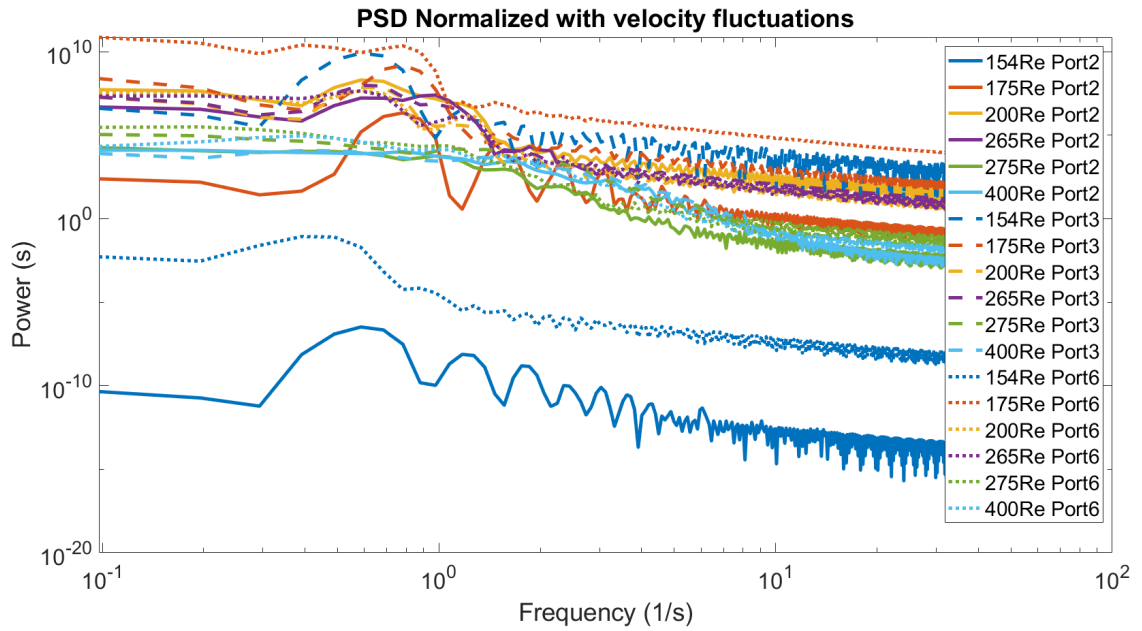places at one side of the channel.
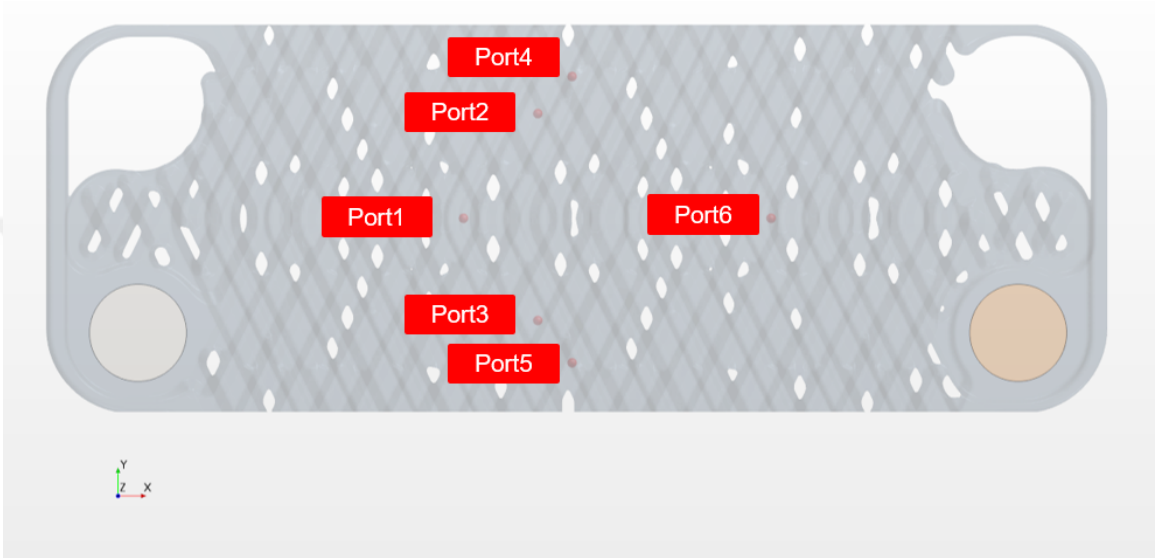
(a)
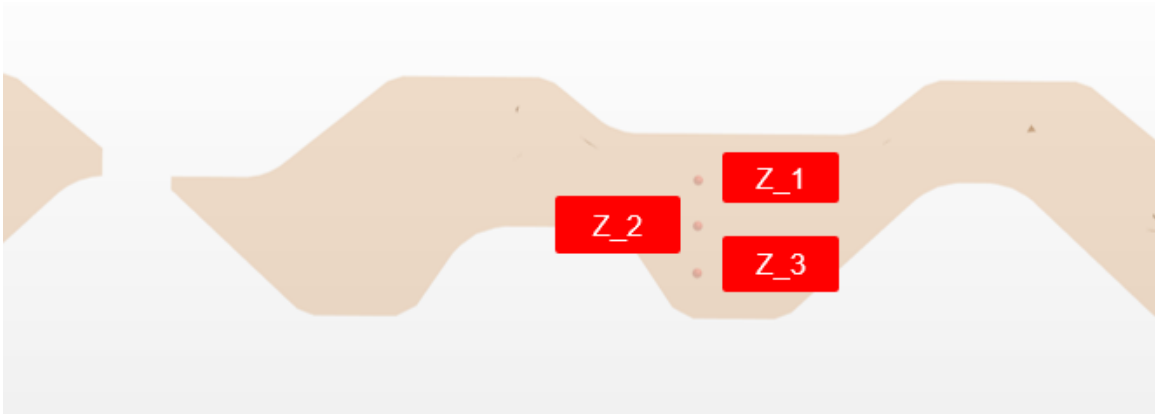
(b)

Figure 30: Velocity measurement points (XY plane); (b) points in z direction

Figure 31: (a)Power spectral density distribution, (b)Normalized power spectral density distribution

Re / Turbulent intensity	Port1	Port2	Port 3
154 Re	0.0212	0.0024	8.93E-04
175 Re	0.0976	0.004	6.57E-04
200 Re	0.0087	0.0197	0.0171
265 Re	0.121	0.0128	0.0214
275 Re	0.4198	0.2618	0.201
400 Re	0.3178	0.3073	0.2315

Figure 32: Turbulent intensity vs. Re
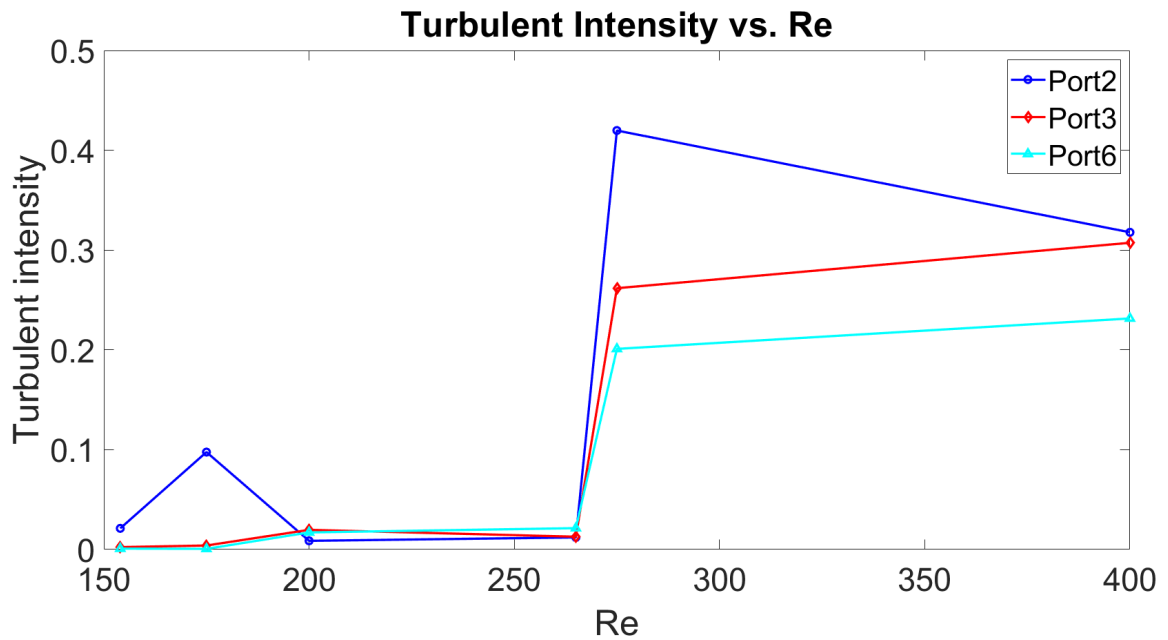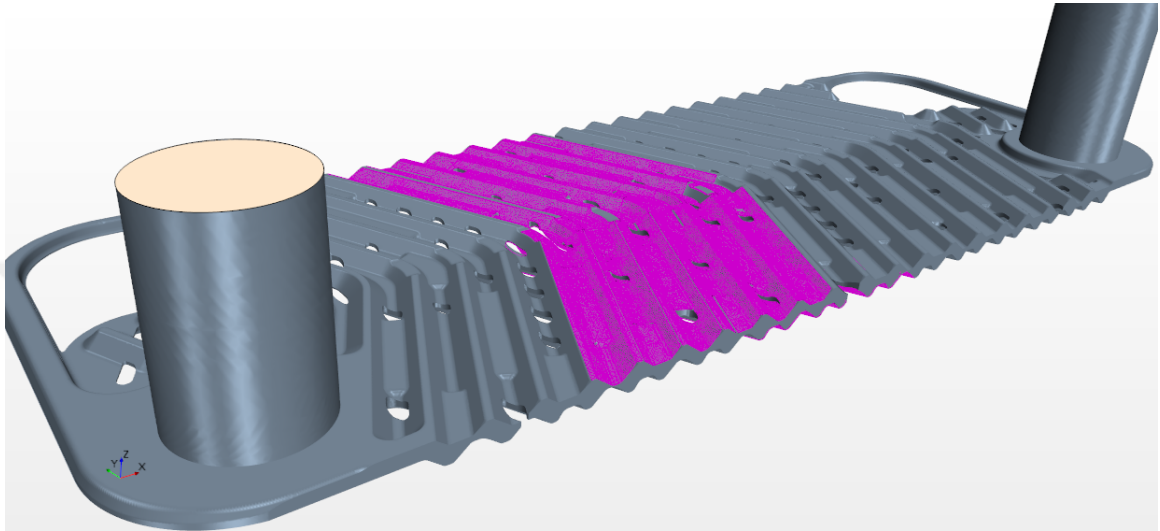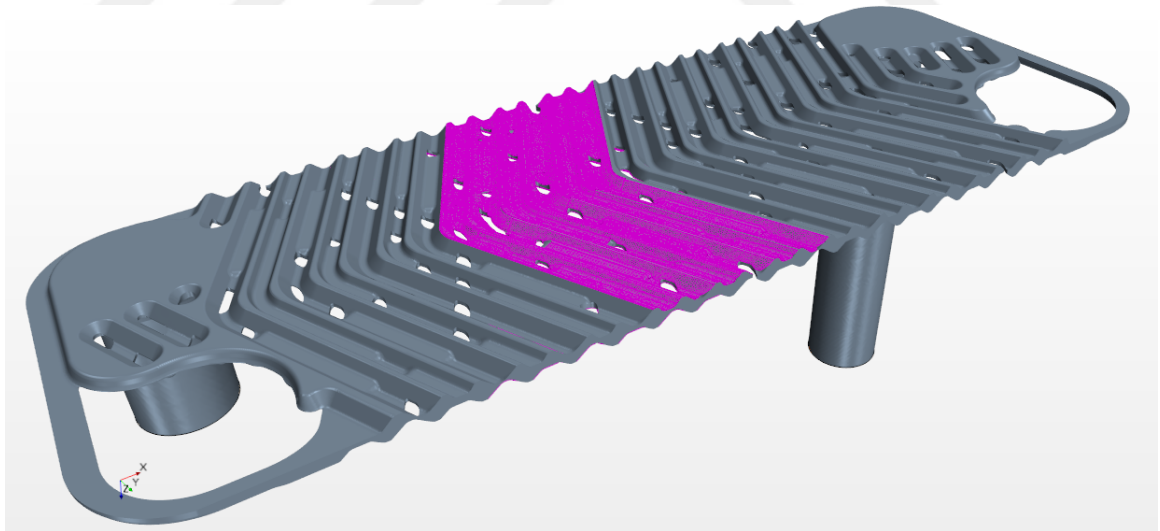

Figure 33: Turbulent intensity

(a)

(b)

Figure 34: Passive scalar introduction regions (a) top (b) bottom
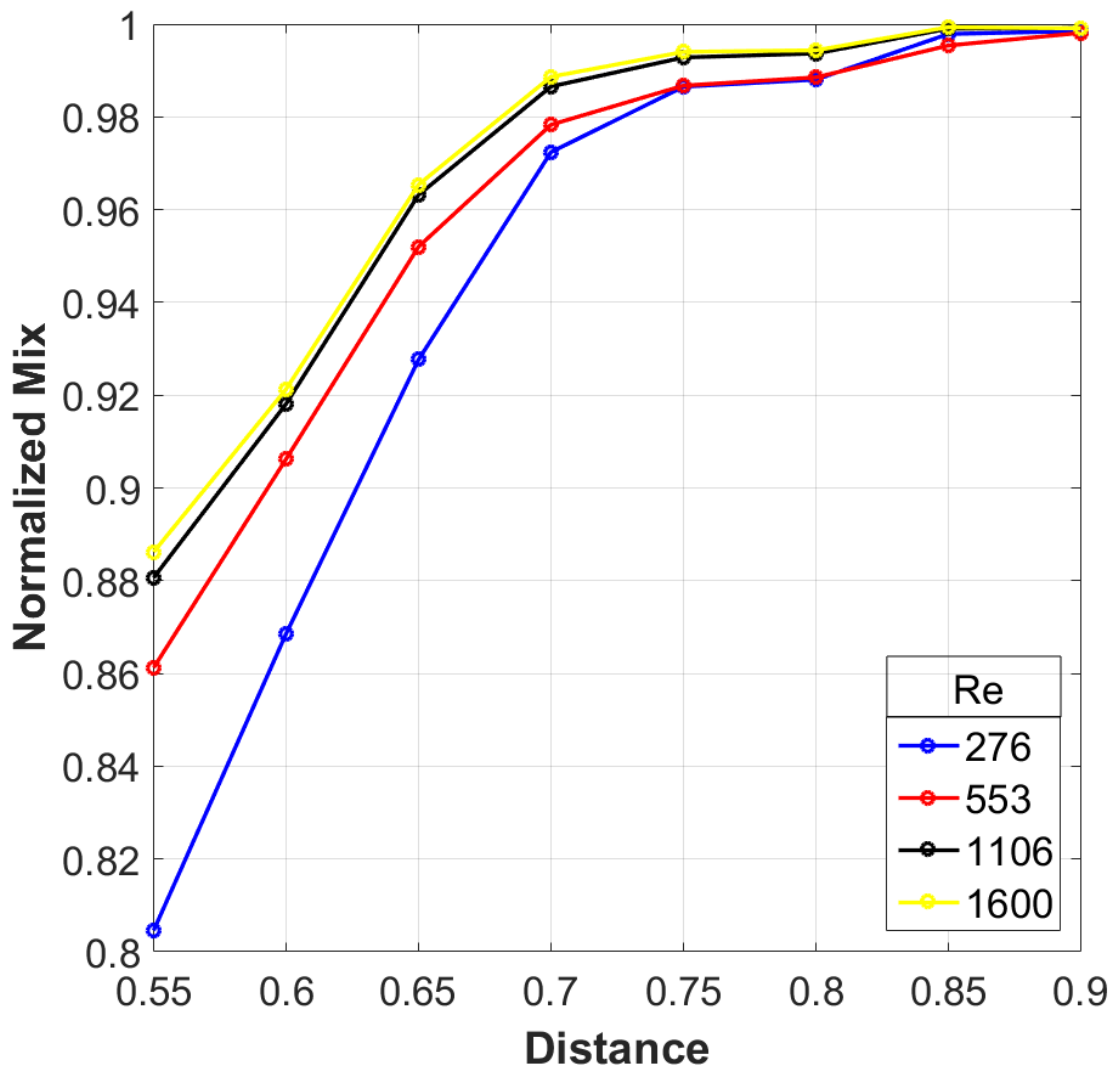
Figure 35: Normalized mixing vs. Distance

(a)

(b)

(c)

(d)

(e)

(f)

(g)

(h)

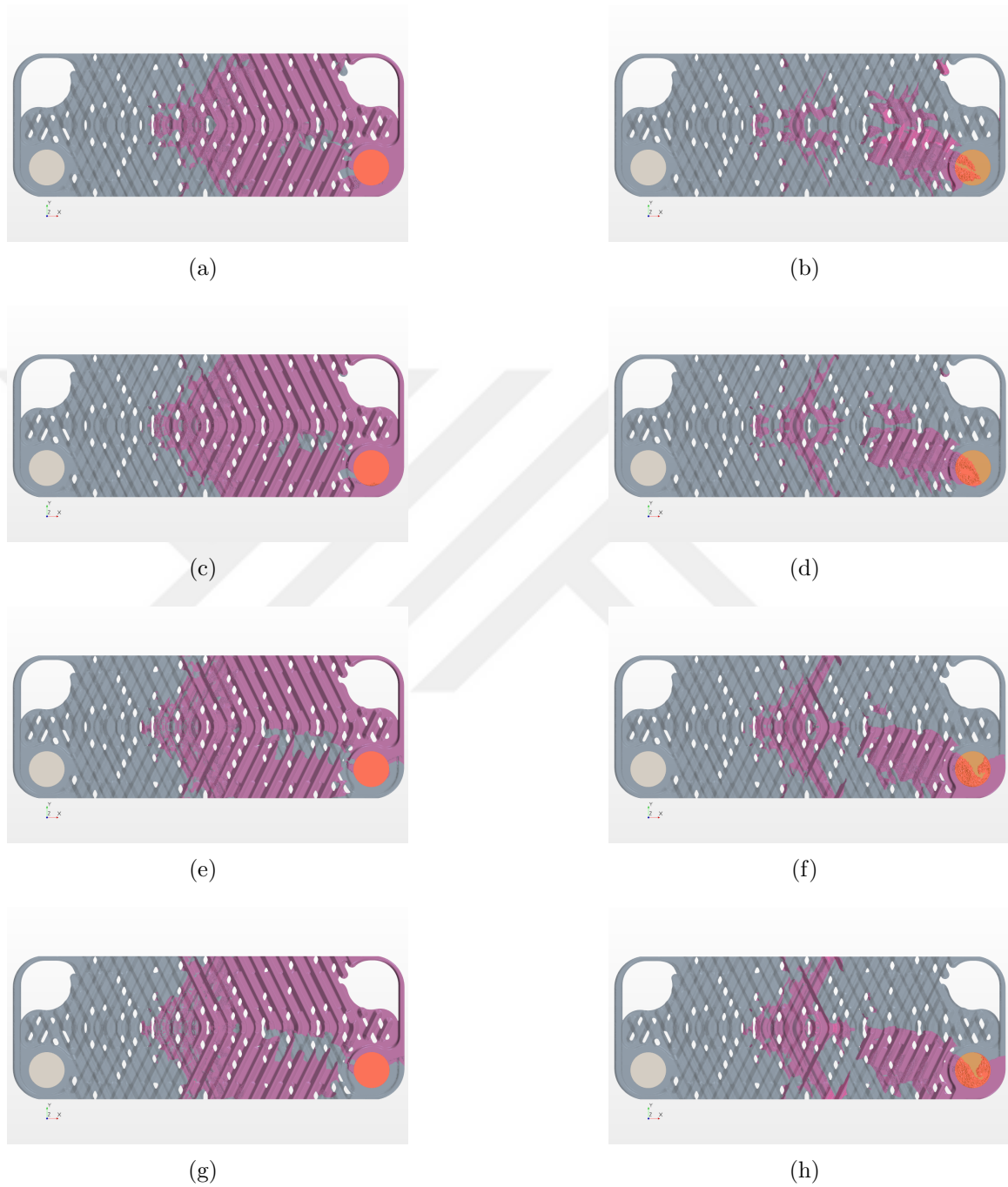**Figure 36:** Visualization of mixing based on ranges of threshold of normalized mixing
(a) at Re = 276, threshold range 0.8-1.00; (b) at Re = 276, threshold range 1.01-5;
(c) at Re = 553, threshold range 0.8-1.00; (d) at Re = 553, threshold range 1.01-5;
(e) at Re = 1106, threshold range 0.8-1.00; (f) at Re = 1106, threshold range 1.01-5;
(g) at Re = 1600, threshold range 0.8-1.00;(h) at Re = 1600, threshold range 1.01-5

CHAPTER V

DISCUSSION AND CONCLUSION

This work consists of visualization experiments, pressure drop measurements, flow rate measurements and LES estimations. The experiments conducted between 100-2800 Re range.

Friction factor which are calculated from the experimental data has two different trends at before and after Re = 500.

Flow visualizations exhibit, that there is no pure cross or helical flow structures occurred in the CPHE channel used in this work. There is a combination of cross and helical flow structures in the channel. At Re= 166 observed flow is steady, however, at higher Res flow becomes unsteady and the flow direction of injected dye oscillates between corrugation and longitudinal direction. Another observation made was separation zones and wakes at brazing points.

LES estimates the friction factor accurate at turbulent region with max 5 percent. Streamlines from LES have similar when it is compared to visualizations.

Numerical results, turbulent intensities change significantly between Re = 265 and Re = 275. Also the PSD graph exhibit that PSD analysis before Re = 265 and after has a significant change. Both results showed that when Re $\geq$ 275 the flow is turbulent and between Re = 265 and Re = 275 there is a transition.

In future, it is planned to conduct Laser doppler anemometer experiments. Measuring local velocities inside the channel at several locations and investigate channel transition.

Bibliography

[Ayub, 2003] Ayub, Z. H. (2003). Plate heat exchanger literature survey and new heat transfer and pressure drop correlations for refrigerant evaporators. *Heat Transfer Engineering*, 24(5):3–16.

[Blomerius et al., 1999] Blomerius, H., Hölsken, C., and Mitra, N. K. (1999). Numerical Investigation of Flow Field and Heat Transfer in Cross-Corrugated Ducts. *Journal of Heat Transfer*, 121(May 1999):314–321.

[Ciofalo et al., 1996] Ciofalo, M., Stasiek, J., and Collins, M. (1996). Investigation of flow and heat transfer in corrugated passagesII. Numerical simulations. *International Journal of Heat and Mass Transfer*, 39(1):165–192.

[Croce and D'Agaro, 2002] Croce, G. and D'Agaro, P. (2002). Numerical analysis of forced convection in plate and frame heat exchangers. *International Journal of Numerical Methods for Heat and Fluid Flow*, 12(6):756–771.

[Doo et al., 2012] Doo, J., Ha, M., Min, J., Stieger, R., Rolt, A., and Son, C. (2012). An investigation of cross-corrugated heat exchanger primary surfaces for advanced intercooled-cycle aero engines (Part-I: Novel geometry of primary surface). *International Journal of Heat and Mass Transfer*, 55(19-20):5256–5267.

[Dović et al., 2009] Dović, D., Palm, B., and Švaić, S. (2009). Generalized correlations for predicting heat transfer and pressure drop in plate heat exchanger channels of arbitrary geometry. *International Journal of Heat and Mass Transfer*, 52(19-20):4553–4563.

[Dović and Švaić, 2007] Dović, D. and Švaić, S. (2007). Influence of chevron plates geometry on performances of plate heat exchangers. *Tehnicki Vjesnik*, 14:37–45.

[Durmu et al., 2009] Durmu, A., Benli, H., Kurtba, I., and Gül, H. (2009). Investigation of heat transfer and pressure drop in plate heat exchangers having different surface profiles. *International Journal of Heat and Mass Transfer*, 52(5-6):1451–1457.

[Focke, 1983] Focke, W. W. (1983). Turbulent Convective Transfer In Plate Heat Exchangers. *International Communications in Heat Mass Tranfer*, 10:201–210.

[Focke and Knibbe, 1986] Focke, W. W. and Knibbe, P. G. (1986). Flow visualization in parallel-plate ducts with corrugated walls. *Journal of Fluid Mechanics*, 165:73–77.

[Focke et al., 1985] Focke, W. W., Zachariades, J., and Olivier, I. (1985). The effect of the corrugation inclination angle on the thermohydraulic performance of plate heat exchangers. *International Journal of Heat and Mass Transfer*, 28(8):1469–1479.

[Gaiser and Kottke, 1990] Gaiser, G. and Kottke, V. (1990). Visualization of flow phenomena and local heat and mass transfer in corrugated passages. *Chemical Engineering Technology*, 12:400–405.

[Gullapalli and Sundén, 2014] Gullapalli, V. S. and Sundén, B. (2014). Cfd simulation of heat transfer and pressure drop in compact brazed plate heat exchangers. *Heat Transfer Engineering*, 35(4):358–366.

[Han et al., 2011] Han, W., Saleh, K., Aute, V., Ding, G., Hwang, Y., and Radermacher, R. (2011). Numerical simulation and optimization of single-phase turbulent flow in chevron-type plate heat exchanger with sinusoidal corrugations. *HVAC&R Research*, 17(2):186–197.

[Jeong et al., 2009] Jeong, J. Y., ki Hong, H., Kim, S. K., and Kang, Y. T. (2009). Impact of plate design on the performance of welded type plate heat exchangers for sorption cycles. *International Journal of Refrigeration*, 32(4):705–711.

[Kakaç and Liu, 2002] Kakaç, S. and Liu, H. (2002). *Heat exchangers: Selection, Rating and Thermal Design.* CRC Press, 2 edition.

[Kanaris et al., 2009] Kanaris, A. G., Mouza, A. A., and Paras, S. V. (2009). Optimal design of a plate heat exchanger with undulated surfaces. *International Journal of Thermal Sciences*, 48(6):1184–1195.

[Khan et al., 2010] Khan, T. S., Khan, M. S., Chyu, M. C., and Ayub, Z. H. (2010). Experimental investigation of single phase convective heat transfer coefficient in a corrugated plate heat exchanger for multiple plate configurations. *Applied Thermal Engineering*, 30(8-9):1058–1065.

[Kim et al., 2010] Kim, M., Baik, Y.-J., Park, S.-R., Ra, H.-S., and Lim, H. (2010). Experimental study on corrugated cross flow air cooled plate heat exchangers. *Experimental Thermal and Fluid Science*, 34:1265–1272.

[Martin, 1996] Martin, H. (1996). A theoretical approach to predict the performance of chevron-type plate heat exchangers. *Chemical Engineering and Processing: Process Intensification*, 35(4):301–310.

[Metwally and Manglik, 2004] Metwally, H. M. and Manglik, R. M. (2004). Enhanced heat transfer due to curvature-induced lateral vortices in laminar flows in sinusoidal corrugated-plate channels. *International Journal of Heat and Mass Transfer*, 47(10-11):2283–2292.

[Muley and Manglik, 1999] Muley, A. and Manglik, R. M. (1999). Experimental Study of Turbulent Flow Heat Transfer and Pressure Drop in a Plate Heat Exchanger With Chevron Plates.

[Nicoud and Ducros, 1999] Nicoud, F. and Ducros, F. (1999). Subgrid-scale stress modelling based on the square of the velocity gradient tensor. *Flow, Turbulence and Combustion*, 62(3):183–200.

[Sarraf et al., 2015] Sarraf, K., Launay, S., and Tadrist, L. (2015). International Journal of Thermal Sciences Complex 3D- fl ow analysis and corrugation angle effect in plate heat exchangers. *International Journal of Thermal Sciences*, 94:126–138.

[Wang et al., 2007] Wang, L., Sunden, B., and Manglik, R. (2007). *Plate Heat Exchangers: Design, applications and performance.*

[Zhang et al., 2019] Zhang, J., Zhu, X., Mondejar, M. E., and Haglind, F. (2019). A review of heat transfer enhancement in plate heat exchangers. *Renewable and Sustainable Energy Reviews*, 101(November 2018):305–328.

[Zhang and Che, 2011] Zhang, L. and Che, D. (2011). Influence of corrugation profile on the thermalhydraulic performance of cross-corrugated plates. *Numerical Heat Transfer; Part A: Applications*, 59(4):267–296.

[Zhang et al., 2016] Zhang, Y., Jiang, C., Yang, Z., Zhang, Y., and Bai, B. (2016). Numerical study on heat transfer enhancement in capsule-type plate heat exchangers. *Applied Thermal Engineering*, 108:1237–1242.

[Zimmerer et al., 2002] Zimmerer, C., Gschwind, P., Gaiser, G., and Kottke, V. (2002). Comparison of heat and mass transfer in different heat exchanger geometries with corrugated walls. *Experimental Thermal and Fluid Science*, 26(2-4):269–273.

VITA

Erdem Peçenek obtained his Mechanical Engineering BSc degree from Özyeğin University in 2016. His final project was Design and Comissioning of Spray Diagnostic Setup. He joined Fluid Mechanics Group in 2016. Currently continues his MSc degree in Özyeğin University, his thesis topic is Numerical and Experimental Investigations on Chevron Type Compact Plate Heat Exchangers.